Master's Thesis

Development of Chemical Tools for Identifying an Inter-Relationship among Multiple Pathological Factors in Alzheimer's Disease

Mingeun Kim

Department of Chemistry

Graduate School of UNIST

2019

Development of Chemical Tools for Identifying an Inter-Relationship among Multiple Pathological Factors in Alzheimer's Disease

Mingeun Kim

Department of Chemistry

Graduate School of UNIST

Development of Chemical Tools for Identifying an Inter-Relationship among Multiple Pathological Factors in Alzheimer's Disease

A thesis submitted to the Graduate School of UNIST
in partial fulfillment of the requirements
for the degree of Master of Science

Mingeun Kim

12. 03. 2018
Approved by

Advisor
Associate Professor Oh-Hoon Kwon

Development of Chemical Tools for Identifying an Inter-Relationship among Multiple Pathological Factors in Alzheimer's Disease

Mingeun Kim

This certifies that the thesis of Mingeun Kim is approved.

12. 03. 2018

Signature

Advisor: Associate Professor Oh-Hoon Kwon

Signature

Associate Professor Mi Hee Lim

Signature

Assistant Professor Jung-Min Kee

Abstract

Alzheimer's disease (AD), which is one of the neurodegenerative diseases, is the most common form of dementia. The general symptoms associated with AD include memory loss, cognitive impairment, and loss of identity. Although much research has been conducted to elucidate the etiology of AD and develop a drug for curing the disease, it has been very challenging due to its complex nature. The accumulation of aggregated amyloid-β (Aβ) peptides is observed as a pathological hallmark in the AD-affected brain. In addition, other pathological features [*e.g.*, dyshomeostasis of metal ions and overproduction of reactive oxygen species (ROS) leading to oxidative stress] are also shown in the brain of AD. Moreover, it has been reported that these pathological elements, including Aβ peptides, metal ions, and ROS could be interconnected with each other. For instance, redox-active metal ions can accelerate the rate of Aβ aggregation and stabilize the toxic Aβ aggregates, such as structured oligomers. Furthermore, redox-active metal ions are able to interact with Aβ species forming metal-bound Aβ (metal–Aβ) complexes that can generate ROS through Fenton-like reactions. Therefore, in order to effectively treat AD, it is necessary to elucidate an inter-relationship among multiple pathogenic factors. The studies presented in this thesis exhibit the development of chemical tools for targeting and regulating multiple pathogenic components found in the brain of AD. Chapter 1 describes a minimalistic redox-based design strategy for engineering compact molecules based on a simplest aromatic framework, benzene, with multi-reactivity against multiple pathological factors of AD. In Chapter 2, investigations of fluorescent probes for monitoring metal ions in biological systems are summarized. Collectively, our overall studies and findings, presented in this thesis, demonstrate the feasibility of establishing effective and efficient design strategies to target and regulate multiple factors found in AD in order to reveal their possible inter-related pathological network.

Table of Contents

Abstract....IV
Table of Contents....V
List of Tables....VII
List of Schemes....VIII
List of Figures....IX
List of Abbreviations....XIV

Chapter 1. Minimalistic Design Approach for Multi-Reactivity against Free Radicals and Metal-Free and Metal-Bound Amyloid-β Peptides: Redox-Based Substitutions of Benzene

1.1. Introduction....2
1.2. Results and Discussion....4
1.2.1. Rational Design Principle and Redox Properties of Small Molecules with Multi-Reactivity....4
1.2.2. Scavenging Capacity of **1**–**10** against Free Organic Radicals....9
1.2.3. Modulatory Effects of **1**–**10** towards Aggregation of Both Metal-free Aβ and Metal–Aβ....10
1.2.4. Oxidative Transformation of **1**–**10** in the Absence and Presence of Aβ and Metal Ion....16
1.2.5. Interactions of **1**–**5** with Metal-free Aβ or Metal–Aβ....23
1.2.6. Bioapplicability of **1**–**4**....26
1.2.7. *In Vivo* Efficacies of **1** and **BQ** towards Aβ Accumulation and Cognitive Function in 5XFAD Mice....28
1.3. Conclusion....32
1.4. Experimental Section....33
1.4.1. Materials and Methods....33
1.4.2. Cyclic Voltammetry....33
1.4.3. Trolox Equivalent Antioxidant Capacity (TEAC) Assay....34
1.4.4. Aβ Aggregation Experiments....34
1.4.5. Gel Electrophoresis with Western Blotting (Gel/Western blot)....35
1.4.6. Transmission Electron Microscopy (TEM)....35
1.4.7. UV–Vis Spectroscopy....35
1.4.8. Docking Studies....36
1.4.9. Electrospray Ionization–Mass Spectrometry (ESI–MS)....36
1.4.10. Matrix-assisted Laser Desorption Ionization–Mass Spectrometry (MALDI–MS)....36
1.4.11. Cell Viability Studies....36
1.4.12. Metabolic Stability....37

1.4.13. Brain Uptake Studies....37
1.4.14. *In Vivo* Efficacies....38
1.5. Acknowledgments....38
1.6. References....39
Chapter 2. Detection of Metal Ions by Fluorescent Probes in Living Cells
2.1. Introduction....44
2.2. Results and Discussion....44
2.2.1. Turn-on Fluorescent Probe, **DHIC**, for Zn^{2+} in Living Cells....44
2.2.2. Turn-on Fluorescent Probe, **ATA-DAS**, for Zn^{2+} in Living Cells....45
2.2.3. Turn-on Fluorescent Probe, **TPH-Jul**, for Al^{3+} in Living Cells....46
2.3. Conclusion....47
2.4. Experimental Section....47
2.4.1. Imaging Experiments in Living Cells....47
2.5. Acknowledgments....48
2.6. References....48
Acknowledgments....49
Curriculum Vitae....50

List of Tables

Table 1.1. Electrochemical analysis of **1**–**10** in DMSO.

Table 1.2. Metabolic stability of **1**–**4**.

Table 1.3. Concentrations of **1** in plasma, brain, and cerebrospinal fluid (CSF) after its 5 min administration in male CD1 mice [10 mg/kg; per os (*p.o.*) injection].

Table 1.4. Change in the body weights of 5XFAD mice during the 30-repeated administrations of **1** and **BQ** [1 mg/kg/day; intraperitoneal (*i.p.*) injection].

List of Schemes

Scheme 2.1. A proposed mechanism of the **DHIC**–Zn^{2+} complex.

Scheme 2.2. A proposed mechanism of the **ATA-DAS**–Zn^{2+} complex.

Scheme 2.3. A proposed mechanism of the **TPH-Jul**–Al^{3+} complex.

List of Figures

Figure 1.1. Overview of a rational strategy of designing small molecules targeting multiple pathogenic factors found in the AD-affected brain and the chemical series (**Group-I** and **Group-II**) studied in this work. (a) Structures of **Group-I** (**1**–**4**) and **Group-II** (**5**–**10**) and the tendency of their oxidation potentials. **1**, Benzene-1,4-diamine; **2**, 4-aminophenol; **3**, N^1,N^1,N^4,N^4-tetramethylbenzene-1,4-diamine; **4**, 4-(dimethylamino)phenol; **5**, aniline; **6**, 4-aminobenzoic acid; **7**, pyridin-4-amine; **8**, *N*,*N*-dimethylaniline; **9**, 4-(dimethylamino)benzoic acid; **10**, *N*,*N*-dimethylpyridin-4-amine. (b) Summary of the multiple targets, desired *in vitro* activities, and *in vivo* efficacies.

Figure 1.2. Oxidation potentials of **1**–**10**, measured by cyclic voltammetry. (a) Cyclic voltammograms of **1**–**4** in DMSO. (b) Values of the first oxidation potential (E_{pa1}) and (c) order of oxidation potentials of **1**–**10** (scan rate at 250 mV/s; DMSO). Conditions: [compound] = 1 mM; [$TBAPF_6$] = 0.1 M (for supporting electrolyte and reference electrode); [$AgNO_3$] = 0.01 M (for reference electrode); N_2 (g); scan rates = 25, 50, 100, 150, 200, and 250 mV/s; three electrodes: glassy carbon working electrode, Ag/Ag(I) reference electrode, and platinum counter electrode; room temperature.

Figure 1.3. Analysis of the cyclic voltammograms of **1**–**4**. Plot of the current (i_{pa} and i_{pc}) as a function of (scan rate)$^{1/2}$ ($v^{1/2}$), indicating the quasi-reversible couple of **1**, **2**, and **4** as well as the reversible couples of **3**. Conditions: [compound] = 1 mM; [$TBAPF_6$] = 0.1 M (for supporting electrolyte and reference electrode); [$AgNO_3$] = 0.01 M (for reference electrode); N_2 (g); scan rates = 25, 50, 100, 150, 200, and 250 mV/s; three electrodes: glassy carbon working electrode, Ag/Ag(I) reference electrode, and platinum counter electrode; room temperature.

Figure 1.4. Cyclic voltammograms of **5**–**10** in DMSO. Conditions: [compound] = 1 mM; [$TBAPF_6$] = 0.1 M (for supporting electrolyte and reference electrode); [$AgNO_3$] = 0.01 M (for reference electrode); N_2 (g); scan rates = 25, 50, 100, 150, 200, and 250 mV/s; three electrodes: glassy carbon working electrode, Ag/Ag(I) reference electrode, and platinum counter electrode; room temperature.

Figure 1.5. Scavenging capability of compounds against free organic radicals, determined by the TEAC assay employing cell lysates. The TEAC values are relative to that of an analog of vitamin E, Trolox (6-hydroxy-2,5,7,8-tetramethylchroman-2-carboxylic acid). The error bars indicate the standard error from four independent experiments. *TEAC values of **5**–**10** were not obtained due to no measurable capacity to quench free radicals.

Figure 1.6. Effects of **1**–**5** on the formation of metal-free or metal-induced $A\beta_{40}$ aggregates. (a) Scheme

of the inhibition experiments. (b-d) Gel/Western blots (an Aβ antibody, 6E10) of the $A\beta_{40}$ species generated in the (b) absence and (c and d) presence of metal ions. Lanes: (C) $A\beta_{40}$; (**1**) $A\beta_{40}$ + **1**; (**2**) $A\beta_{40}$ + **2**; (**3**) $A\beta_{40}$ + **3**; (**4**) $A\beta_{40}$ + **4**; (**5**) $A\beta_{40}$ + **5**. (e) TEM images of the samples obtained from (b) metal-free $A\beta_{40}$ and $A\beta_{40}$ with 1 equiv of (c) Cu(II) and (d) Zn(II). Conditions: [$A\beta_{40}$] = 25 μM; [Cu(II) or Zn(II)] = 12.5, 25, and 50 μM; [compound] = 50 μM; 20 mM HEPES, pH 7.4 [for metal-free or Zn(II)-containing samples] or pH 6.6 [for Cu(II)-added samples], 150 mM NaCl; 37 °C; 24 h; constant agitation. Scale bar = 200 nm.

Figure 1.7. Influence of **1**–**5** on preformed metal-free or metal-associated $A\beta_{40}$ aggregates. (a) Scheme of the disaggregation experiments. (b-d) Gel/Western blots (6E10) of the $A\beta_{40}$ species generated in the (b) absence and (c and d) presence of metal ions. Lanes: (C) $A\beta_{40}$; (**1**) $A\beta_{40}$ + **1**; (**2**) $A\beta_{40}$ + **2**; (**3**) $A\beta_{40}$ + **3**; (**4**) $A\beta_{40}$ + **4**; (**5**) $A\beta_{40}$ + **5**. (e) TEM images of the samples obtained from (b) metal-free $A\beta_{40}$ and $A\beta_{40}$ with 1 equiv of (c) Cu(II) and (d) Zn(II). Conditions: [$A\beta_{40}$] = 25 μM; [Cu(II) or Zn(II)] = 12.5, 25, and 50 μM; [compound] = 50 μM; 20 mM HEPES, pH 7.4 [for metal-free or Zn(II)-containing samples] or pH 6.6 [for Cu(II)-added samples], 150 mM NaCl; 37 °C; 24 h; constant agitation. Scale bar = 200 nm.

Figure 1.8. Impact of **1**–**5** on formation of metal-free or metal-induced $A\beta_{42}$ aggregates. (a) Scheme of the inhibition experiments. (b-d) Gel/Western blots (6E10) of the $A\beta_{42}$ species generated in the (b) absence and (c and d) presence of metal ions. Lanes: (C) $A\beta_{42}$; (**1**) $A\beta_{42}$ + **1**; (**2**) $A\beta_{42}$ + **2**; (**3**) $A\beta_{42}$ + **3**; (**4**) $A\beta_{42}$ + **4**; (**5**) $A\beta_{42}$ + **5**. (e) TEM images of the samples obtained from (b) metal-free $A\beta_{42}$ and $A\beta_{42}$ with 1 equiv of (c) Cu(II) and (d) Zn(II). Conditions: [$A\beta_{42}$] = 25 μM; [Cu(II) or Zn(II)] = 12.5, 25, and 50 μM; [compound] = 50 μM; 20 mM HEPES, pH 7.4 [for metal-free or Zn(II)-containing samples] or pH 6.6 [for Cu(II)-added samples], 150 mM NaCl; 37 °C; 24 h; constant agitation. Scale bar = 200 nm.

Figure 1.9. Influence of **1**–**5** on preformed metal-free or metal-induced $A\beta_{42}$ aggregates. (a) Scheme of the disaggregation experiments. (b-d) Gel/Western blots (6E10) of the $A\beta_{42}$ species generated in the (b) absence and (c and d) presence of metal ions. Lanes: (C) $A\beta_{42}$; (**1**) $A\beta_{42}$ + **1**; (**2**) $A\beta_{42}$ + **2**; (**3**) $A\beta_{42}$ + **3**; (**4**) $A\beta_{42}$ + **4**; (**5**) $A\beta_{42}$ + **5**. (e) TEM images of the samples obtained from (b) metal-free $A\beta_{42}$ and $A\beta_{42}$ with 1 equiv of (c) Cu(II) and (d) Zn(II). Conditions: [$A\beta_{42}$] = 25 μM; [Cu(II) or Zn(II)] = 12.5, 25, and 50 μM; [compound] = 50 μM; 20 mM HEPES, pH 7.4 [for metal-free or Zn(II)-containing samples] or pH 6.6 [for Cu(II)-added samples], 150 mM NaCl; 37 °C; 24 h; constant agitation. Scale bar = 200 nm.

Figure 1.10. Effects of **6**–**10** on metal-free or metal-induced $A\beta_{40}$ and $A\beta_{42}$ aggregation pathways. (a)

Scheme of the inhibition and disaggregation experiments. (b and c) Analysis of the resultant (b) $A\beta_{40}$ and (c) $A\beta_{42}$ species by gel/Western blot (6E10). Lanes: (C) $A\beta_{40/42}$; (**6**) $A\beta_{40/42}$ + **6**; (**7**) $A\beta_{40/42}$ + **7**; (**8**) $A\beta_{40/42}$ + **8**; (**9**) $A\beta_{40/42}$ + **9**; (**10**) $A\beta_{40/42}$ + **10**. Conditions: [$A\beta_{40/42}$] = 25 μM; [Cu(II) or Zn(II)] = 25 μM; [compound] = 50 μM; 20 mM HEPES, pH 7.4 [for metal-free or Zn(II)-containing samples] or pH 6.6 [for Cu(II)-added samples], 150 mM NaCl; 37 °C; 24 h; constant agitation.

Figure 1.11. Analyses of **1**'s transformation and interaction with metal-free $A\beta_{40}$ or Cu(II)-associated $A\beta_{40}$ as well as proposed mechanisms. (a) Transfiguration of **1** in the presence of $A\beta_{40}$ with or without Cu(II), detected by UV–Vis spectroscopy. Conditions: [$A\beta_{40}$] = 25 μM; [Cu(II)] = 25 μM; [**1**] = 50 μM; 20 mM HEPES, pH 7.4 (for metal-free samples) or pH 6.6 [for Cu(II)-added samples], 150 mM NaCl; 37 °C; 0–24 h; no agitation. (b-d) Interactions of **1** with metal-free $A\beta_{40}$ and Cu(II)-treated $A\beta_{40}$, analyzed by ESI–MS, ESI–MS^2, and MALDI–MS. $A\beta_{40}$ monomer incubated with **1** in the (b and d) absence and (d) presence of Cu(II) was detected by (b) ESI–MS or (d) MALDI–MS. Oxidized $A\beta_{40}$ and an adduct between $A\beta_{40}$ and oxidatively transformed **1** (*i.e.*, **BQ**) are indicated with red and blue circles, respectively. The covalent bond with $A\beta_{40}$ (green circle) was only observed from **1**-treated samples. (c) ESI–MS^2 spectrum of the singly oxidized $A\beta_{40}^{4+}$ produced upon addition of **1**. Conditions (for ESI–MS studies): [$A\beta_{40}$] = 50 μM; [**1**] = 100 μM; 1 mM ammonium acetate, pH 7.4; 37 °C; 24 h; no agitation. The samples were diluted by 10 fold with ddH_2O before injection to the mass spectrometer. Conditions (for MALDI–MS measurements): [$A\beta_{40}$] = 25 μM; [Cu(II)] = 25 μM; [**1**] = 50 μM; pH 7.4 (for metal-free samples) or pH 6.6 [for Cu(II)-added samples]; 37 °C; 24 h; constant agitation. (e) Two proposed pathways: (left) peptide oxidation by **1**; (right) Formation of a covalent adduct between Aβ and oxidatively transformed **1** (*i.e.*, **BQ**).

Figure 1.12. Transformation of **1**–**10** in the absence and presence of $A\beta_{40}$ with or without metal ions, detected by UV–Vis spectroscopy. Conditions: [$A\beta_{40}$] = 25 μM; [Cu(II) or Zn(II)] = 25 μM; [compound] = 50 μM; 20 mM HEPES, pH 7.4 [for metal-free or Zn(II)-containing samples] or pH 6.6 [for Cu(II)-added samples], 150 mM NaCl; 37 °C; 0-24 h; no agitation.

Figure 1.13. Docking studies of **1**–**5** with $A\beta_{40}$ monomer (PDB 2LFM). (a) Docked conformations of compounds with $A\beta_{40}$ (surface and zoon-in images). Hydrogen bonding between compounds and $A\beta_{40}$ is indicated with gray dashed lines (2.2-2.7 Å). The self-recognition site in $A\beta_{40}$ is highlighted in yellow. (b) Binding energy of the compounds with $A\beta_{40}$ monomer.

Figure 1.14. Interactions of **1**–**5** with metal-free and metal-treated $A\beta_{40}$. $A\beta_{40}$ monomer incubated (a)

with **2**–**5** in the absence of metal ions and (b) with **1** in presence of Zn(II) was monitored by (a) ESI–MS and (b) MALDI–MS. Oxidized ions of $A\beta_{40}$ and $A\beta_{40}$–**BQ** adducts are indicated with red and blue circles, respectively. The covalent adducts between $A\beta_{40}$ and oxidatively transformed **1**–**4** (*i.e.*, **BQ**) are indicated with green circles. Conditions (for ESI–MS studies): [$A\beta_{40}$] = 50 μM; [compound] = 100 μM; 1 mM ammonium acetate, pH 7.4; 37 °C; 24 h; no agitation. The samples were diluted by 10 fold with ddH_2O before injection to the mass spectrometer. Conditions (for MALDI–MS measurements): [$A\beta_{40}$] = 25 μM; [Zn(II)] = 25 μM; [**1**] = 50 μM; pH 7.4; 37 °C; 24 h; constant agitation.

Figure 1.15. Cytotoxicity of **1**–**4**. Cell viability (%) of N2a cells incubated with various concentrations of **1**–**4** was obtained by the MTT assay. Error bars indicate the standard error from four independent experiments. Conditions: [compound] = 5, 10, 25, and 50 μM (1 % v/v DMSO); 37 °C; 24 h.

Figure 1.16. Analysis of the amounts of Aβ species in **1**- or **BQ**-treated 5XFAD mice. (a) Levels of soluble $A\beta_{42}$, insoluble $A\beta_{42}$, total $A\beta_{42}$, and oligomeric Aβ were analyzed in triplicate per sample by ELISA. Lanes: (Vehicle) 5XFAD + vehicle; (**BQ**) 5XFAD + **BQ**; (**1**) 5XFAD + **1**. (b) Loads of amyloid deposits and plaques in the brain expressed as the percent area of 4G8-immunoreactive deposits or the number of congophilic plaques per mm^2 of a region of interest, which was taken from hippocampal (*hip*), cortical (*ctx*) and thalamic (*tlm*) areas. (c) Representative images of 4G8-immunoreactive (1^{st} row) or Congo red-positive (2^{nd} and 3^{rd} rows) amyloid deposits or plaques in *hip* and *ctx* (1^{st} and 3^{rd} rows), or *tlm* (2^{nd} row) regions in the brains of vehicle- (1^{st} column), **BQ**- (2^{nd} column), or **1**-treated (3^{rd} column) 5XFAD mice are shown. Congo red stained brain sections were also counter-stained with haematoxylin to differentiate the nuclei of neural cells (2^{nd} and 3^{rd} rows). Subiculum (*sub*), corpus callosum (*cc*), and fornix (*fx*). Scale bars = 500 μm (white) or 200 μm (black). The measurements were performed in five sagittal sections taken every 200 μm from midline per animal. Bars denote mean ± standard errors of mean (s.e.m.) (animal numbers; n = 19 for vehicle-treated 5XFAD mice; n = 9 for **BQ**-treated 5XFAD mice; n = 12 for **1**-treated 5XFAD mice). $^{*}P < 0.05$, or $^{**}P < 0.01$ by unpaired two-tail *t*-test.

Figure 1.17. Measurement of spatial learning and memory improvements in **1**- or **BQ**-administrated 5XFAD mice. (a) Escape latency time daily assessed for five days from the day of the 30^{th} compound treatment in the Morris water maze (MWM) test. From the 2^{nd} training trial to the 5^{th} trial, the latency time became significantly shorter in non-transgenic wild-type mice (WT; $P = 0.012$ by one-way ANOVA with Student-Newman-Keuls post hoc test) or **1**-treated 5XFAD mice (**1**; $P = 0.0017$), but not in vehicle- (Vehicle; $P = 0.054$) or **BQ**-treated (**BQ**; $P = 0.40$) 5XFAD mice. (b) After the MWM test, the probe trials were performed in the same water pool in the absence of the scape platform. All images present the representative paths of the mice to search for the previous platform location [the small circle

area in the gray, northwest (NW) target quadrant] for 60 s (from point S to point E). (c-f) In the probe test, we recorded (c) the path distance to first enter the target quadrant, (d) the latency time to touch the previous location of the platform, (e) the crossing frequency to traverse across the target platform, and (f) the times spent in the target quadrant to search for the platform. Lanes: (WT) wild-type; (Vehicle) 5XFAD + vehicle; (**BQ**) 5XFAD + **BQ**; (**1**) 5XFAD + **1**. The statistical comparisons were performed between vehicle-treated 5XFAD and their wild-type littermate mice (∗) or between vehicle- and **1**-treated 5XFAD mice (#). Bars denote mean ± s.e.m. (animal numbers; n = 17 for wild-type mice; n = 19 for vehicle-treated 5XFAD mice; n = 9 for **BQ**-treated 5XFAD mice; n = 12 for **1**-treated 5XFAD mice). $^{*,\#}P < 0.05$, $^{**,\#\#}P < 0.01$, or $^{***,\#\#\#}P < 0.001$ by unpaired two-tail *t*-test.

Figure 2.1. Fluorescent imaging of **DHIC** for Zn^{2+} with or without S^{2-} in HeLa cells. (a) The cells were pre-incubated with **DHIC** for 1 h prior to treatment with Zn^{2+}. (b) The cells incubated with **DHIC** for 1 h were treated with Zn^{2+} for 1 h. Conditions: [**DHIC**] = 20 μM; [Zn^{2+}] = 600 μM; [S^{2-}] = 400 μM; 37 °C; 5% CO_2. The scale bar is 50 μm.

Figure 2.2. Fluorescent imaging of **ATA-DAS** for Zn^{2+} in HeLa cells. The cells were incubated with **ATA-DAS** and Zn^{2+} for 10 min. Conditions: [**ATA-DAS**] = 30 μM; [Zn^{2+}] = 5 mM; 37 °C; 5% CO_2. The scale bar is 50 μm.

Figure 2.3. Fluorescent imaging of **TPH-Jul** for Al^{3+} in HeLa cells. The cells were incubated with **TPH-Jul** with various concentrations of Al^{3+} for 2 h. Conditions: [**TPH-Jul**] = 10 μM; [Al^{3+}] = 0.25, 0.5, 1, and 1.5 mM; 37 °C; 5% CO_2. The scale bar is 50 μm.

List of Abbreviations

ABTS	2,2'-azino-bis(3-ethylbenzthiazoline-6-sulphonic acid)
Aβ	Amyloid-β
AD	Alzheimer's disease
APP	Amyloid precursor protein
BBB	Blood-brain barrier
BQ	*p*-Benzoquinone
BQDI	*p*-Benzoquinonediimine
cc	Corpus callosum
CID	Collision induced dissociation
Clint	Intrinsic clearance
CSF	Cerebrospinal fluid
ctx	Cortical
CV	Cyclic voltammetry
DMEM	Dulbecco's Modified Eagle Medium
DMF	Dimethylformamide
DMSO	Dimethyl sulfoxide
DNA	Deoxyribonucleic acid
$E_{1/2}$	Half wave potential
E_{pa}	Anodic peak potential
ELISA	Enzyme-linked immunosorbent assay
ESI–MS	Electrospray ionization–mass spectrometry
ESI–MS^2	Tandem mass spectrometry
FA	Formic acid
fx	Fornix
Gel/Western blot	Gel electrophoresis with Western blot
GFP	Green fluorescence protein
hAPP	Human amyloid precursor protein
HEPES	4-(2-Hydroxyethyl)-1-piperazineethanesulfonic acid
hip	Hippocampal
His	Histidine
i	Current
i.p.	Intraperitoneal injection
ν	Scan rate
LC-MS/MS	Liquid chromatograph triple quadrupole mass spectrometer

LM	Low mass
MALDI–MS	Matrix-assisted laser desorption ionization–mass spectrometry
Metal–Aβ	Metal-bound Aβ
Met	Methionine
MS	mass spectrometry
MTT	3-(4,5-Dimethyl-2-thiazolyl)-2,5-diphenyl-2*H*-tetrazolium bromide
MWM	Morris water maze
MW	Molecular weight
N_2	Dinitrogen
N2a	Murine neuroblastoma Neuro-2a
NADPH	Dihydronicotinamide adenine dinucleotide phosphate
NMR	Nuclear magnetic resonance spectroscopy
NW	Northwest
oAβ	Oligomeric Aβ
Opti-MEM	Opti-Minimal Essential Medium
PBS	Phosphate buffered saline
PDB	Protein Data Bank
p.o.	Per os
PSEN1	Presenilin-1
R.O.I.	Regions of interest
ROS	Reactive oxygen species
SDS	Sodium dodecyl sulfate
s.e.m.	Standard errors of mean
sub	Subiculum
$t_{1/2}$	Half-life
TBAPF6	Tetrabutylammonium hexafluorophosphate
TBS	Tris-buffered saline
TBS-T	Tris-buffered saline containing 0.1% Tween-20
TEAC	Trolox equivalent antioxidant capacity
TEM	Transmission electron microscopy
tlm	Thalamic
Trolox	6-Hydroxy-2,5,7,8-tetramethylchroman-2-carboxylic acid
UV–Vis	UV–Visible spectroscopy
WT	Wild-type

Chapter 1.

Minimalistic Design Approach for Multi-Reactivity against Free Radicals and Metal-Free and Metal-Bound Amyloid-β Peptides: Redox-Based Substitutions of Benzene

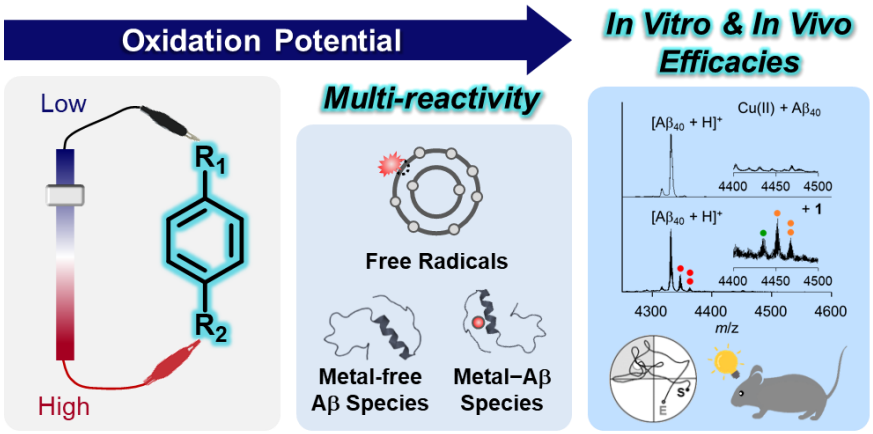

I thank Juhye Kang and Misun Lee for cyclic voltammetry, gel/Western blot, UV–Vis spectroscopy, docking studies, and cell experiments; Jiyeon Han for ESI–MS; Dr. Hyuck Jin Lee and Eunju Nam for TEM; Eunyoung Tak, Min Sun Kim, Doin Kim, and Professor Joo-Yong Lee for *in vivo* studies employing 5XFAD mice with data analysis; Geewoo Nam for writing of paper; Dr. Shin Jung Lee for MALDI–MS. I carried out the experiments using the TEAC assay, gel/Western blot, UV–Vis spectroscopy, cell experiments, data analysis, and writing, along with organization of all data.

1.1. Introduction

Generation of reactive oxygen species (ROS) is an inevitable consequence of cellular metabolism.[1] Intracellular ROS is tightly regulated through biological scavenging mechanisms utilizing a range of enzymes and antioxidants.[1] Under normal conditions, in which the production and removal of ROS are balanced, ROS are involved in critical cellular processes, such as signal transduction and gene transcription.[2-4] A shift in balance resulting in the overproduction of free radicals, however, can damage lipids, proteins, and DNA leading to oxidative stress.[1,2,5]

The brain envelops a substantial amount of ROS as a product of the heightened O_2 metabolism, high metal ion content, and deficient antioxidant capacity.[6,7] At the cellular level, neurons exhibit an exceptional vulnerability against oxidative stress, which arises from its radical sensitive membrane and high membrane surface area to cytoplasmic volume ratio.[8] Thus, oxidative stress is implicated as a central factor in the progression of neurodegeneration as observed in Alzheimer's disease (AD), Parkinson's disease, and amyotrophic lateral sclerosis.[5,9-12] Clinical efforts to extensively prevent oxidative damage against AD employing natural antioxidants, including vitamin C and E, failed to demonstrate significant therapeutic efficacy in stopping the progress of the disease, however.[13,14] Such observations have led researchers to recognize the complex multifactorial nature of AD.[13,14]

Redox chemistry among pathogenic elements found in AD [*e.g.*, ROS, amyloid-β (Aβ), and metal ions] denotes inter-connections among the proposed hypotheses regarding its etiopathology: oxidative stress, amyloid cascade, and metal ion.[5,11,15-22] For instance, ROS are reported to promote the cerebral deposition of Aβ, the aggregation-prone peptide constituent of senile plaques, by increasing its production and diminishing its degradation and clearance.[23,24] In addition, ROS mediate Aβ-induced neurotoxicity.[15,25] Redox-active metal ions, highly accumulated in senile plaques of the AD-affected brain, can also generate ROS and coordinate to Aβ peptides to form metal-bound Aβ (metal–Aβ) complexes that are also capable of forming ROS through Fenton-like reactions.[5,11,22,26-28]

To advance our understanding of the pathological relationships among ROS, Aβ, and metal ions, research efforts have been dedicated towards developing multifunctional chemical reagents that can target and regulate these pathogenic factors of AD.[10,29-31] Numerous reports of multifunctional molecules presented a structure-based design strategy by linking, fusing, and incorporating previously published molecular frameworks exhibiting desired biological and chemical properties (*e.g.*, antioxidant capacity, Aβ interaction, and metal chelation).[10,30,31] In contrast, a structure-mechanism-based design strategy, which considers both chemical structures and mechanistic reactivity with targets, has been increasingly reported as a strategy to design multifunctional compounds, with the suggestion regarding a correlation between redox activity and multifunctionality.[32-34]

Herein, we report compact molecules (Figure 1.1a), devised from the smallest aromatic backbone, benzene, with multi-reactivity against free radicals, metal-free Aβ, and metal–Aβ constructed through

a minimalistic redox-based design strategy. Only minor structural variations on benzene, including *p*-substitution, were applied to tune its electronic properties. In addition, an inherent relationship between redox activity and multifunctionality was established and confirmed utilizing our series of strategically designed small molecules (**1**–**10**). The redox-active compounds (**Group-I**; Figure 1a, left) illustrated regulatory activities against free radicals, metal-free Aβ, and metal–Aβ *in vitro*. The representative molecule of the study, **1**, further demonstrated its ability to reduce Aβ accumulation and ameliorate cognitive deficits *in vivo* (Figure 1.1b). Our detailed mechanistic studies confirmed a redox-dependent trend regarding the molecules' ability to interact and react with free radicals, metal-free Aβ, and metal–Aβ. Collectively, the presented work validates the feasibility of converging multiple reactivities in a single structural entity by tuning the oxidation potential of a simple backbone through minor structural variations, without any structural complexity. In addition, our findings provide new insight towards designing multi-reactive chemicals and contribute towards the efficient and effective development of synthetic agents to elucidate the convoluted pathology of AD.

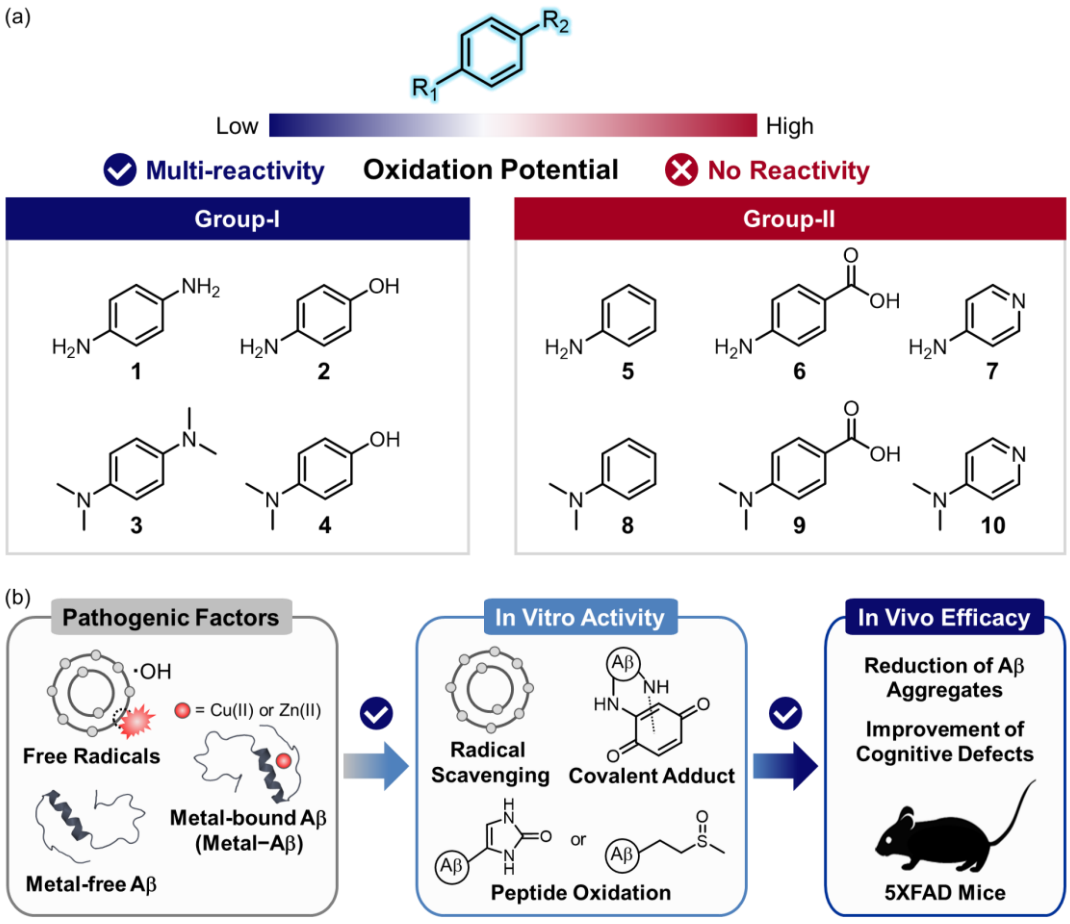

Figure 1.1. Overview of a rational strategy of designing small molecules targeting multiple pathogenic factors found in the AD-affected brain and the chemical series (**Group-I** and **Group-II**) studied in this

work. (a) Structures of **Group-I** (**1**–**4**) and **Group-II** (**5**–**10**) and the tendency of their oxidation potentials. **1**, Benzene-1,4-diamine; **2**, 4-aminophenol; **3**, N^1,N^1,N^4,N^4-tetramethylbenzene-1,4-diamine; **4**, 4-(dimethylamino)phenol; **5**, aniline; **6**, 4-aminobenzoic acid; **7**, pyridin-4-amine; **8**, *N*,*N*-dimethylaniline; **9**, 4-(dimethylamino)benzoic acid; **10**, *N*,*N*-dimethylpyridin-4-amine. (b) Summary of the multiple targets, desired *in vitro* activities, and *in vivo* efficacies.

1.2. Results and Discussion

1.2.1. Rational Design Principle and Redox Properties of Small Molecules with Multi-Reactivity

Redox-active compounds have recently been reported for their utility as multifunctional small molecules capable of targeting and regulating more than one pathological factor implicated in the pathology of AD.[32-35] This indicates the significance of redox property as a parameter for engineering such small molecules. This concept, however, has not been fully established. To validate this notion, ten compact molecules were rationally designed based on the benzene scaffold considering the correlation between redox activity and multi-reactivity against multiple pathological factors found in the AD-affected brain (*i.e.*, free radicals, metal-free Aβ, and metal–Aβ). Benzene, the most basic aromatic structure, exhibits relative stability through its rigid sp^2 hybrid structure.[36-38] The structural symmetry of benzene affords a neutral molecular entity with marginal dipole moments influencing its electronic properties, making this molecule an ideal candidate for varying and examining the effects of its electronic distribution on benzene.[39-41] Thus, we conducted various *p*-substitutions (*i.e.*, incorporation of electron-donating or electron-withdrawing groups) onto benzene or replaced benzene with a heterocycle (*i.e.*, pyridine) to build up two groups of small molecules (**Group-I** and **Group-II**; Figure 1.1a) and determine their oxidation potentials and multi-reactivity against free radicals, metal-free Aβ, and metal–Aβ.

Group-I (**1**–**4**), embodying a relatively electron-rich benzene, was specifically constructed to possess two electron-donating groups (*e.g.*, primary amino, dimethyl amino, or hydroxyl group). In contrast, **Group-II** (**5**–**10**) was devised to exhibit a comparatively electron-poor aromatic structure by first introducing an electron-donating group (*i.e.*, primary amino or dimethyl amino group) to afford **5** and **8**. Subsequent incorporation of an electron-withdrawing group (*i.e.*, carboxylate group) yielded **6** and **9**, and replacement of benzene with pyridine produced **7** and **10**. After procuring our library of compact molecules, their oxidation potentials, reactivity against multiple pathological factors of AD *in vitro*, and *in vivo* efficacy in an AD transgenic mouse model were determined (*vide infra*).

The redox properties of **Group-I** and **Group-II** were evaluated by cyclic voltammetry (CV) in DMSO. **Group-I** exhibited quasi-reversible (**1**, **2**, and **4**) or reversible (**3**) redox potential waves (Figures 1.2a and 1.3 and Table 1.1). Oppositely, **Group-II** displayed irreversible redox potential waves (Figure 1.4 and Table 1.1). Therefore, the $E_{1/2}$ values of the compounds could only be obtained from **Group-I** (**1**–**4**; *ca.* 0.14, 0.21, 0.21, and 0.069 V at 250 mV/s, respectively). Moreover, the first anode

potential (E_{pa1}) of **Group-I** (**1**–**4**; *ca.* –0.096, 0.28, –0.054, and 0.20 V at 250 mV/s, respectively; Figure 1.2b) was observed to be significantly lower than those of **Group-II** (**5**–**10**; *ca.* 0.68, 0.60, 0.71, 0.56, 0.56, and 0.66 V at 250 mV/s, respectively; Figure 1.2b). Our CV data indicates that the compounds in **Group-I** undergo oxidation more readily than those in **Group-II** (Figure 1.2c), possibly due to the presence of two electron-donating groups promoting the stabilization of the cationic radical form through electron delocalization.[40,42,43] Our studies confirm our design approach to alter the electronic properties of benzene utilizing minimal structural modifications.

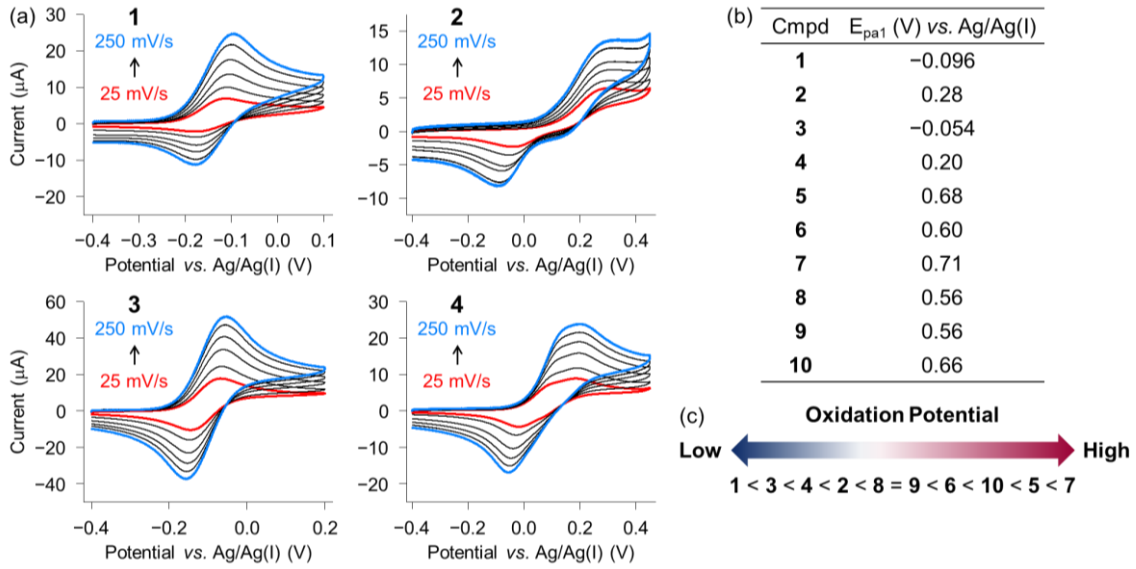

Figure 1.2. Oxidation potentials of **1**–**10**, measured by cyclic voltammetry. (a) Cyclic voltammograms of **1**–**4** in DMSO. (b) Values of the first oxidation potential (E_{pa1}) and (c) order of oxidation potentials of **1**–**10** (scan rate at 250 mV/s; DMSO). Conditions: [compound] = 1 mM; [$TBAPF_6$] = 0.1 M (for supporting electrolyte and reference electrode); [$AgNO_3$] = 0.01 M (for reference electrode); N_2 (g); scan rates = 25, 50, 100, 150, 200, and 250 mV/s; three electrodes: glassy carbon working electrode, Ag/Ag(I) reference electrode, and platinum counter electrode; room temperature.

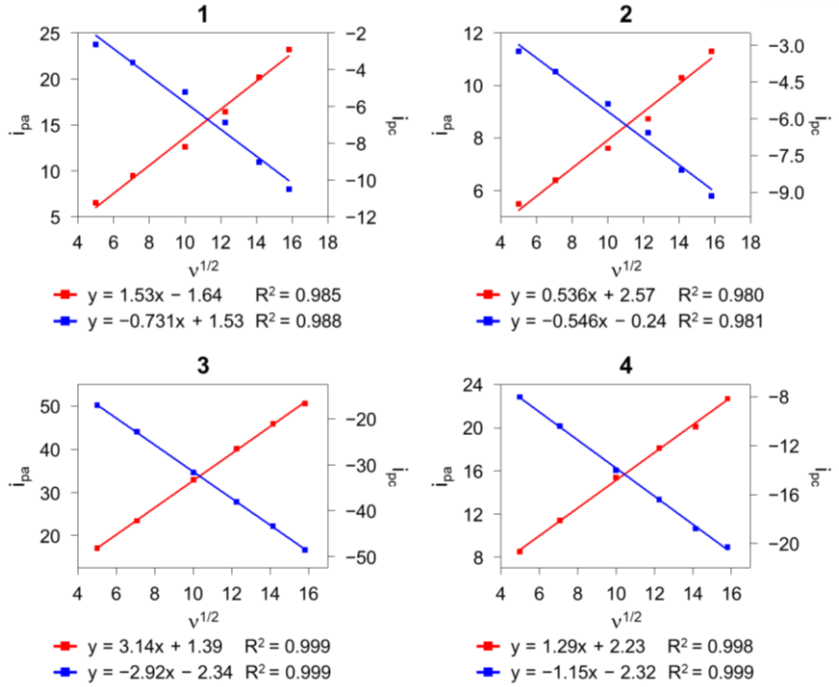

Figure 1.3. Analysis of the cyclic voltammograms of **1**–**4**. Plot of the current (i_{pa} and i_{pc}) as a function of (scan rate)$^{1/2}$ ($\nu^{1/2}$), indicating the quasi-reversible couple of **1**, **2**, and **4** as well as the reversible couples of **3**. Conditions: [compound] = 1 mM; [$TBAPF_6$] = 0.1 M (for supporting electrolyte and reference electrode); [$AgNO_3$] = 0.01 M (for reference electrode); N_2 (g); scan rates = 25, 50, 100, 150, 200, and 250 mV/s; three electrodes: glassy carbon working electrode, Ag/Ag(I) reference electrode, and platinum counter electrode; room temperature.

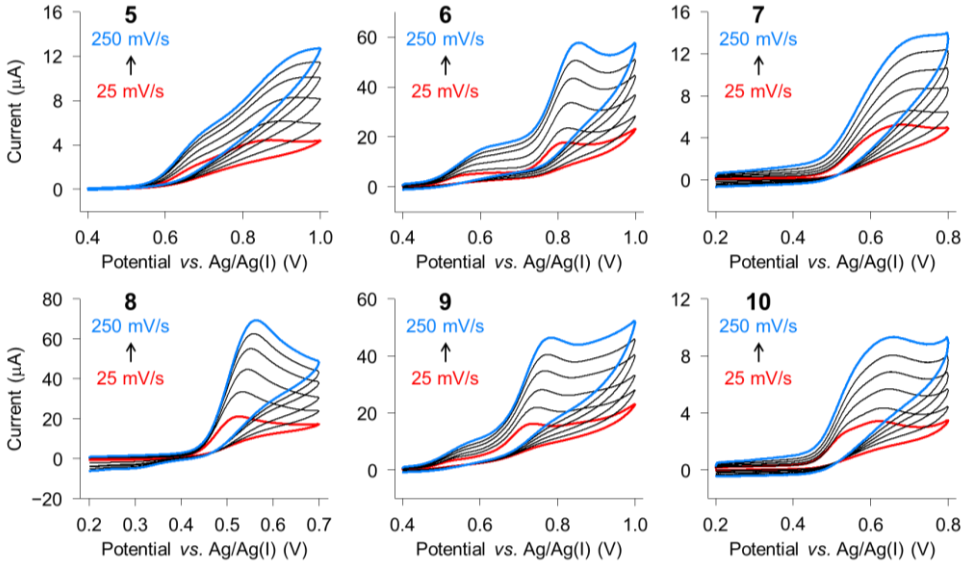

Figure 1.4. Cyclic voltammograms of **5**–**10** in DMSO. Conditions: [compound] = 1 mM; [$TBAPF_6$] =

0.1 M (for supporting electrolyte and reference electrode); [$AgNO_3$] = 0.01 M (for reference electrode); N_2 (g); scan rates = 25, 50, 100, 150, 200, and 250 mV/s; three electrodes: glassy carbon working electrode, Ag/Ag(I) reference electrode, and platinum counter electrode; room temperature.

Table 1.1. Electrochemical analysis of **1**–**10** in DMSO.

1								
Scan Rate (mV/s)	E_{pa1} (V)	E_{pa2} (V)	i_{pa1} (μA)	i_{pa2} (μA)	E_{pc1} (V)	E_{pc2} (V)	i_{pc1} (μA)	i_{pc2} (μA)
25	−0.114	–	6.51	–	−0.177	–	2.61	–
50	−0.109	–	9.47	–	−0.175	–	3.61	–
100	−0.104	–	12.6	–	−0.175	–	5.22	–
150	−0.103	–	16.4	–	−0.175	–	6.86	–
200	−0.101	–	20.2	–	−0.175	–	9.03	–
250	−0.0956	–	23.2	–	−0.178	–	10.5	–
2								
Scan Rate (mV/s)	E_{pa1} (V)	E_{pa2} (V)	i_{pa1} (μA)	i_{pa2} (μA)	E_{pc1} (V)	E_{pc2} (V)	i_{pc1} (μA)	i_{pc2} (μA)
25	0.266	–	5.48	–	0.156	−0.0383	3.25	5.83
50	0.266	–	6.40	–	0.155	−0.0527	4.08	7.73
100	0.270	–	7.61	–	0.154	−0.0696	5.40	10.3
150	0.278	–	8.73	–	0.146	−0.0771	6.57	11.9
200	0.281	–	10.3	–	0.146	−0.0876	8.10	14.7
250	0.283	–	11.3	–	0.143	−0.0905	9.15	16.1
3								
Scan Rate (mV/s)	E_{pa1} (V)	E_{pa2} (V)	i_{pa1} (μA)	i_{pa2} (μA)	E_{pc1} (V)	E_{pc2} (V)	i_{pc1} (μA)	i_{pc2} (μA)
25	−0.0695	–	17.0	–	−0.145	–	17.0	–
50	−0.0651	–	23.4	–	−0.147	–	22.8	–
100	−0.0609	–	32.9	–	−0.150	–	31.7	–
150	−0.0594	–	40.1	–	−0.154	–	38.1	–
200	−0.0572	–	45.9	–	−0.154	–	43.4	–
250	−0.0537	–	50.6	–	−0.156	–	48.6	–
4								
Scan Rate (mV/s)	E_{pa1} (V)	E_{pa2} (V)	i_{pa1} (μA)	i_{pa2} (μA)	E_{pc1} (V)	E_{pc2} (V)	i_{pc1} (μA)	i_{pc2} (μA)
25	0.184	–	8.50	–	−0.0190	–	8.01	–
50	0.190	–	11.4	–	−0.0284	–	10.4	–
100	0.196	–	15.4	–	−0.0391	–	14.0	–
150	0.198	–	18.1	–	−0.0464	–	16.4	–
200	0.197	–	20.1	–	−0.0515	–	18.8	–
250	0.196	–	22.7	–	−0.0574	–	20.3	–

5

Scan Rate (mV/s)	E_{pa1} (V)	E_{pa2} (V)	i_{pa1} (μA)	i_{pa2} (μA)	E_{pc1} (V)	E_{pc2} (V)	i_{pc1} (μA)	i_{pc2} (μA)
25	0.672	0.868	18.9	16.5	–	–	–	–
50	0.673	0.899	23.3	56.9	–	–	–	–
100	0.675	0.930	29.4	77.9	–	–	–	–
150	0.678	0.958	35.3	94.2	–	–	–	–
200	0.678	0.978	36.7	105	–	–	–	–
250	0.680	0.994	40.3	115	–	–	–	–

6

Scan Rate (mV/s)	E_{pa1} (V)	E_{pa2} (V)	i_{pa1} (μA)	i_{pa2} (μA)	E_{pc1} (V)	E_{pc2} (V)	i_{pc1} (μA)	i_{pc2} (μA)
25	0.568	0.808	3.56	14.6	–	–	–	–
50	0.567	0.817	4.25	19.0	–	–	–	–
100	0.588	0.826	6.70	28.7	–	–	–	–
150	0.588	0.835	8.78	38.4	–	–	–	–
200	0.593	0.841	10.2	45.4	–	–	–	–
250	0.604	0.850	10.4	48.1	–	–	–	–

7

Scan Rate (mV/s)	E_{pa1} (V)	E_{pa2} (V)	i_{pa1} (μA)	i_{pa2} (μA)	E_{pc1} (V)	E_{pc2} (V)	i_{pc1} (μA)	i_{pc2} (μA)
25	0.644	–	2.83	–	–	–	–	–
50	0.666	–	5.82	–	–	–	–	–
100	0.685	–	7.62	–	–	–	–	–
150	0.699	–	8.91	–	–	–	–	–
200	0.707	–	10.4	–	–	–	–	–
250	0.710	–	10.9	–	–	–	–	–

8

Scan Rate (mV/s)	E_{pa1} (V)	E_{pa2} (V)	i_{pa1} (μA)	i_{pa2} (μA)	E_{pc1} (V)	E_{pc2} (V)	i_{pc1} (μA)	i_{pc2} (μA)
25	0.525	–	20.0	–	–	–	–	–
50	0.534	–	32.4	–	–	–	–	–
100	0.545	–	43.4	–	–	–	–	–
150	0.552	–	53.7	–	–	–	–	–
200	0.558	–	60.7	–	–	–	–	–
250	0.563	–	65.9	–	–	–	–	–

9

Scan Rate (mV/s)	E_{pa1} (V)	E_{pa2} (V)	i_{pa1} (μA)	i_{pa2} (μA)	E_{pc1} (V)	E_{pc2} (V)	i_{pc1} (μA)	i_{pc2} (μA)
25	0.523	0.722	2.12	13.7	–	–	–	–
50	0.523	0.729	2.83	18.9	–	–	–	–
100	0.541	0.745	3.38	24.2	–	–	–	–
150	0.541	0.753	4.30	30.7	–	–	–	–
200	0.550	0.762	5.41	36.2	–	–	–	–
250	0.557	0.772	5.49	39.7	–	–	–	–

10								
Scan Rate (mV/s)	E_{pa1} (V)	E_{pa2} (V)	i_{pa1} (μA)	i_{pa2} (μA)	E_{pc1} (V)	E_{pc2} (V)	i_{pc1} (μA)	i_{pc2} (μA)
25	0.620	–	2.90	–	–	–	–	–
50	0.630	–	3.82	–	–	–	–	–
100	0.646	–	5.03	–	–	–	–	–
150	0.652	–	6.08	–	–	–	–	–
200	0.654	–	6.94	–	–	–	–	–
250	0.656	–	7.73	–	–	–	–	–

1.2.2. Scavenging Capacity of 1–10 against Free Organic Radicals

The Trolox equivalent antioxidant capacity (TEAC) assay[32-35,44-47] was performed to measure the free radical scavenging ability of **Group-I** and **Group-II**. The cationic radical form of ABTS, $ABTS^{\bullet+}$ [ABTS = 2,2'-azino-bis(3-ethylbenzthiazoline-6-sulphonic acid)], was used as a source of organic free radicals in the medium containing the lysates of murine neuroblastoma Neuro-2a (N2a) cells. The TEAC values represent the radical scavenging capacity of compounds relative to a water-soluble vitamin E analogue, Trolox.[32-35,45,47] As shown in Figure 1.5, **1**–**4** (**Group-I**), observed to have lower oxidation potentials compared to those in **Group-II**, exhibited the substantial radical scavenge capacity comparable (**1**, **2**, and **4**) to or greater (**3**) than that of Trolox. The notable free radical scavenging activity of **3** might stem from the rapid kinetics of its oxidation and stabilization of its radical form.[48,49] The antioxidant capacity of the compounds in **Group-II** could not be determined through the TEAC due to their limited radical scavenging activity. Overall, **Group-I** and **Group-II** demonstrate distinct capabilities to eliminate organic free radicals in a manner correspondent to their oxidation potentials (*vide supra*).

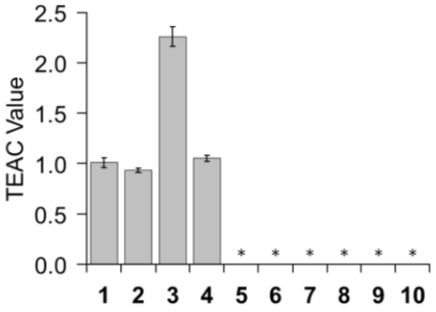

Compound	TEAC Value
1	1.01 ± 0.05
2	0.93 ± 0.02
3	2.26 ± 0.10
4	1.05 ± 0.03

Figure 1.5. Scavenging capability of compounds against free organic radicals, determined by the TEAC

assay employing cell lysates. The TEAC values are relative to that of an analog of vitamin E, Trolox (6-hydroxy-2,5,7,8-tetramethylchroman-2-carboxylic acid). The error bars indicate the standard error from four independent experiments. *TEAC values of **5**–**10** were not obtained due to no measurable capacity to quench free radicals.

1.2.3. Modulatory Effects of 1–10 towards Aggregation of Both Metal-free Aβ and Metal–Aβ.

Aggregation and accumulation of Aβ peptides, produced by enzymatic cleavages of amyloid precursor protein (APP), can induce neurotoxicity in the brain. Thus, Aβ is considered as one of the pathogenic hallmarks of AD.[15,17-20,50] In addition, binding of metal ions [*e.g.*, Cu(II) and Zn(II)] to Aβ can modify its aggregation pathways and also generate toxic Aβ aggregates.[51-54] Therefore, modulating those Aβ aggregation pathways by small molecules is an efficient method for redirecting their on-pathways into less toxic, off-pathway.[32,55,56] To identify the effects of **1**–**10** on the aggregation pathways of both metal-free Aβ and metal–Aβ, the molecular weight (MW) distribution and morphology of the Aβ aggregates, generated by treatment with our compounds, were analyzed through gel electrophoresis with Western blot (gel/Western blot) utilizing an anti-Aβ antibody (6E10) and transmission electron microscopy (TEM), respectively (Figures 1.6-1.10). Inhibition (Figure 1.6a, 1.8a, and 1.10a) and disaggregation experiments (Figures 1.7a, 1.9a, and 1.10a) that can evaluate the compounds' ability to inhibit the aggregation of Aβ peptides or disassemble preformed Aβ aggregates, respectively,[30,32-35,47] were carried out employing $A\beta_{40}$ and $A\beta_{42}$, two major isoforms of Aβ.[15,18,20,34] Smaller Aβ aggregates (*ca.* 1-240 kDa) can appear as dark smearing bands on the images of gel/Western blot. Conversely, larger Aβ aggregates that are not able to penetrate the gel matrix are not observed *via* gel/Western blot. Such aggregates, however, are in general visualized through TEM.

In the inhibition experiments with metal-free $A\beta_{40}$, **1**–**4** (in **Group-I**) noticeably increased the smearing bands from *ca.* 7 to 270 kDa or reduced the intensity of the bands at *ca.* < 7 kDa, compared to the compound-free $A\beta_{40}$ (Figure 1.6b). In the presence of metal ions [*i.e.*, Cu(II) and Zn(II)], the change in the MW distributions of the $A\beta_{40}$ samples treated with **1**–**4** became more prominent (Figure 1.6c,d). Oppositely, **5**–**10** (**Group-II**) did not discernibly alter the MW distributions of both metal-free $A\beta_{40}$ and metal–$A\beta_{40}$ (Figures 1.6b-d and 1.10b). TEM studies demonstrated deviant conformations of metal-free $A\beta_{40}$ and metal–$A\beta_{40}$ aggregates incubated with **1**–**4** from the gel/Western blot experiments. Small and truncated $A\beta_{40}$ fibrils, along with amorphous aggregates suggested to be less toxic than other structured aggregates,[30,32,33] were observed from the samples of **Group-I** presenting a notable conformational contrast from the mature insoluble $A\beta_{40}$ fibrils produced from the samples of compound-free metal-free and metal–Aβ as controls (Figure 1.6e).

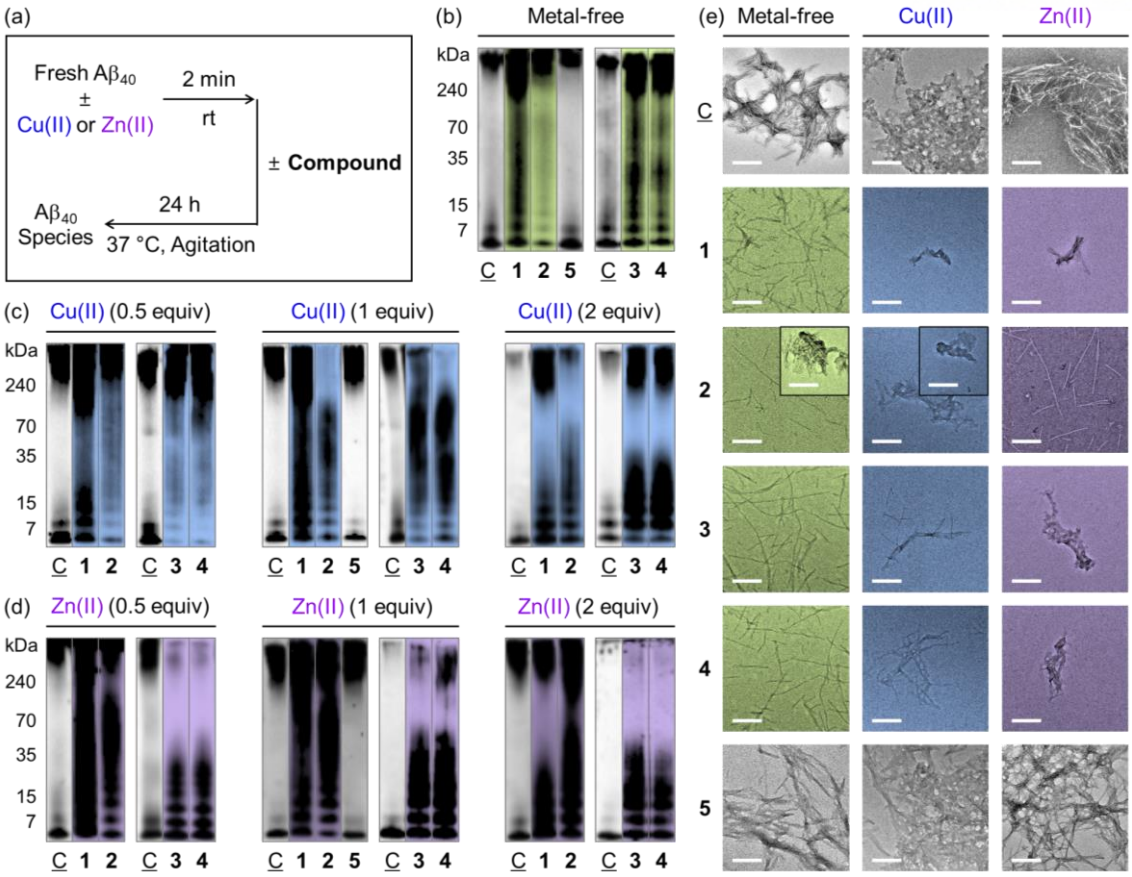

Figure 1.6. Effects of **1**–**5** on the formation of metal-free or metal-induced Aβ$_{40}$ aggregates. (a) Scheme of the inhibition experiments. (b-d) Gel/Western blots (an Aβ antibody, 6E10) of the Aβ$_{40}$ species generated in the (b) absence and (c and d) presence of metal ions. Lanes: (C) Aβ$_{40}$; (**1**) Aβ$_{40}$ + **1**; (**2**) Aβ$_{40}$ + **2**; (**3**) Aβ$_{40}$ + **3**; (**4**) Aβ$_{40}$ + **4**; (**5**) Aβ$_{40}$ + **5**. (e) TEM images of the samples obtained from (b) metal-free Aβ$_{40}$ and Aβ$_{40}$ with 1 equiv of (c) Cu(II) and (d) Zn(II). Conditions: [Aβ$_{40}$] = 25 μM; [Cu(II) or Zn(II)] = 12.5, 25, and 50 μM; [compound] = 50 μM; 20 mM HEPES, pH 7.4 [for metal-free or Zn(II)-containing samples] or pH 6.6 [for Cu(II)-added samples], 150 mM NaCl; 37 °C; 24 h; constant agitation. Scale bar = 200 nm.

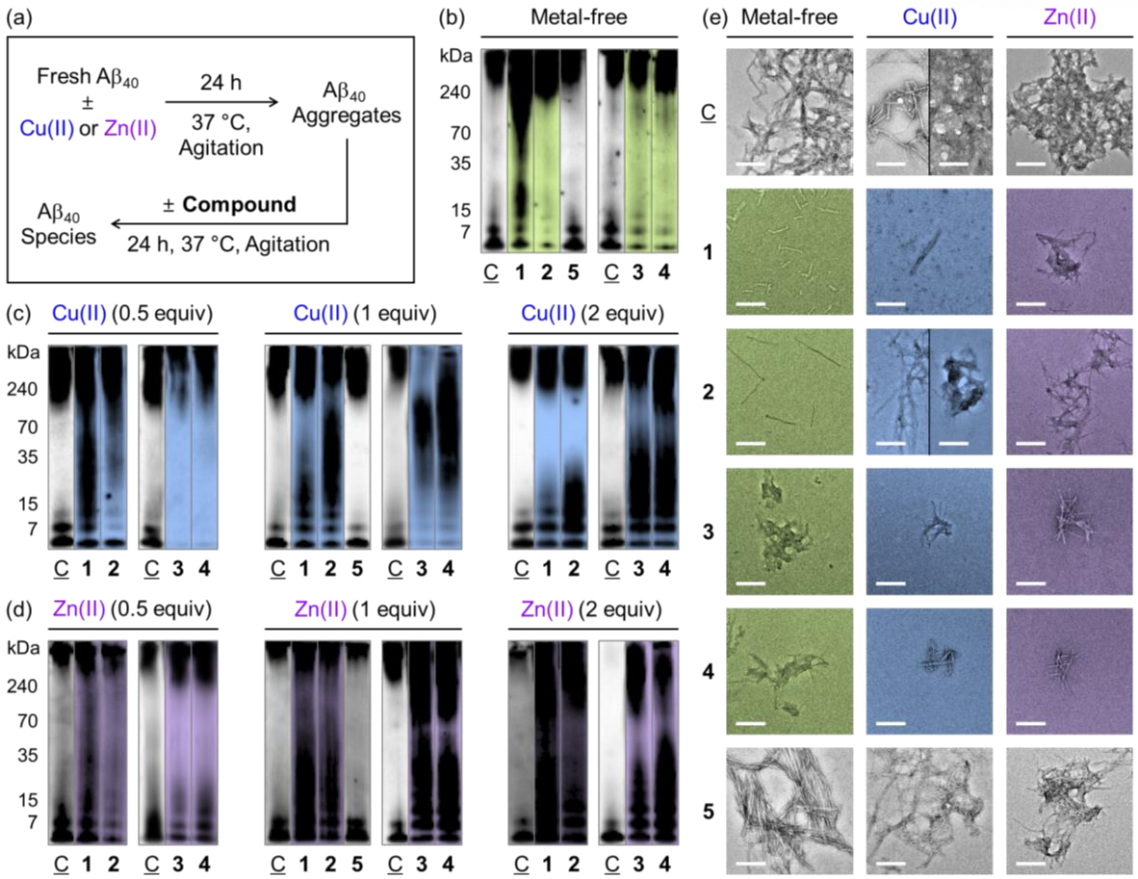

Figure 1.7. Influence of **1**–**5** on preformed metal-free or metal-associated Aβ$_{40}$ aggregates. (a) Scheme of the disaggregation experiments. (b-d) Gel/Western blots (6E10) of the Aβ$_{40}$ species generated in the (b) absence and (c and d) presence of metal ions. Lanes: (C) Aβ$_{40}$; (**1**) Aβ$_{40}$ + **1**; (**2**) Aβ$_{40}$ + **2**; (**3**) Aβ$_{40}$ + **3**; (**4**) Aβ$_{40}$ + **4**; (**5**) Aβ$_{40}$ + **5**. (e) TEM images of the samples obtained from (b) metal-free Aβ$_{40}$ and Aβ$_{40}$ with 1 equiv of (c) Cu(II) and (d) Zn(II). Conditions: [Aβ$_{40}$] = 25 μM; [Cu(II) or Zn(II)] = 12.5, 25, and 50 μM; [compound] = 50 μM; 20 mM HEPES, pH 7.4 [for metal-free or Zn(II)-containing samples] or pH 6.6 [for Cu(II)-added samples], 150 mM NaCl; 37 °C; 24 h; constant agitation. Scale bar = 200 nm.

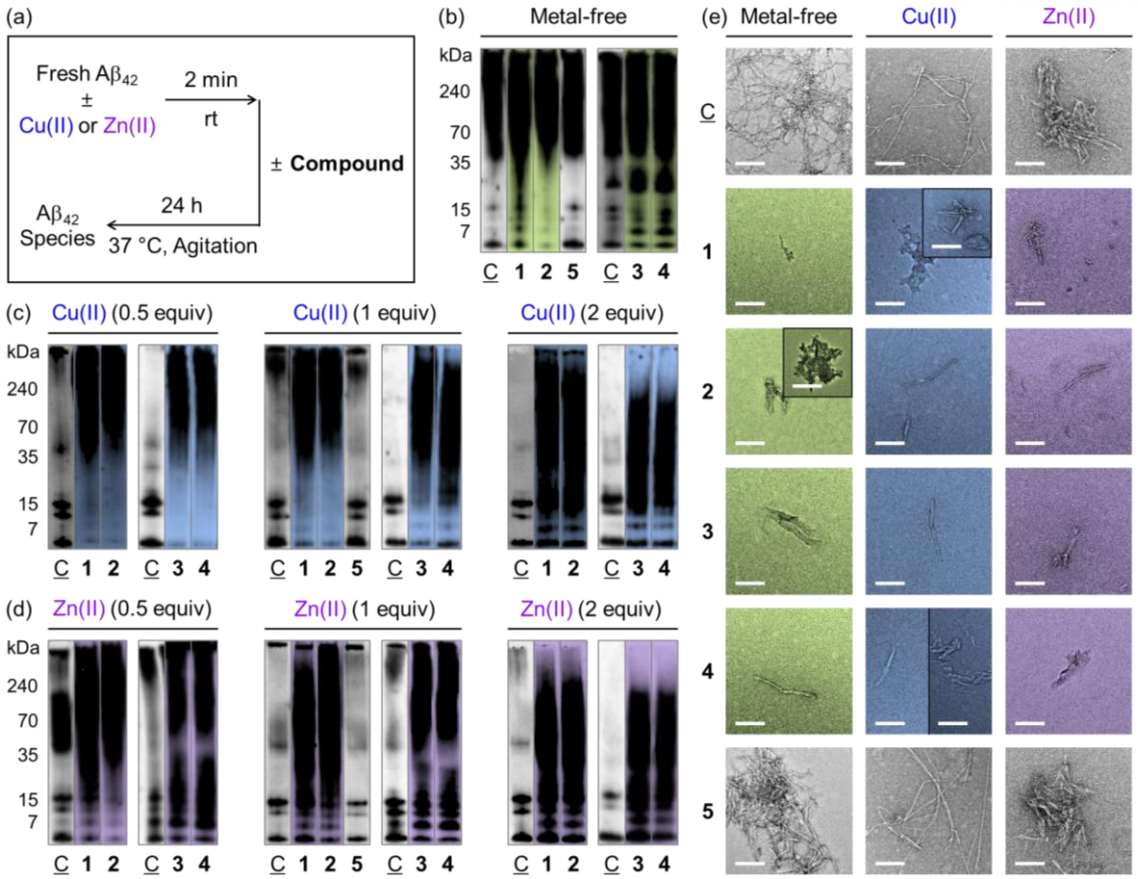

Figure 1.8. Impact of **1**–**5** on formation of metal-free or metal-induced Aβ$_{42}$ aggregates. (a) Scheme of the inhibition experiments. (b-d) Gel/Western blots (6E10) of the Aβ$_{42}$ species generated in the (b) absence and (c and d) presence of metal ions. Lanes: (C) Aβ$_{42}$; (**1**) Aβ$_{42}$ + **1**; (**2**) Aβ$_{42}$ + **2**; (**3**) Aβ$_{42}$ + **3**; (**4**) Aβ$_{42}$ + **4**; (**5**) Aβ$_{42}$ + **5**. (e) TEM images of the samples obtained from (b) metal-free Aβ$_{42}$ and Aβ$_{42}$ with 1 equiv of (c) Cu(II) and (d) Zn(II). Conditions: [Aβ$_{42}$] = 25 μM; [Cu(II) or Zn(II)] = 12.5, 25, and 50 μM; [compound] = 50 μM; 20 mM HEPES, pH 7.4 [for metal-free or Zn(II)-containing samples] or pH 6.6 [for Cu(II)-added samples], 150 mM NaCl; 37 °C; 24 h; constant agitation. Scale bar = 200 nm.

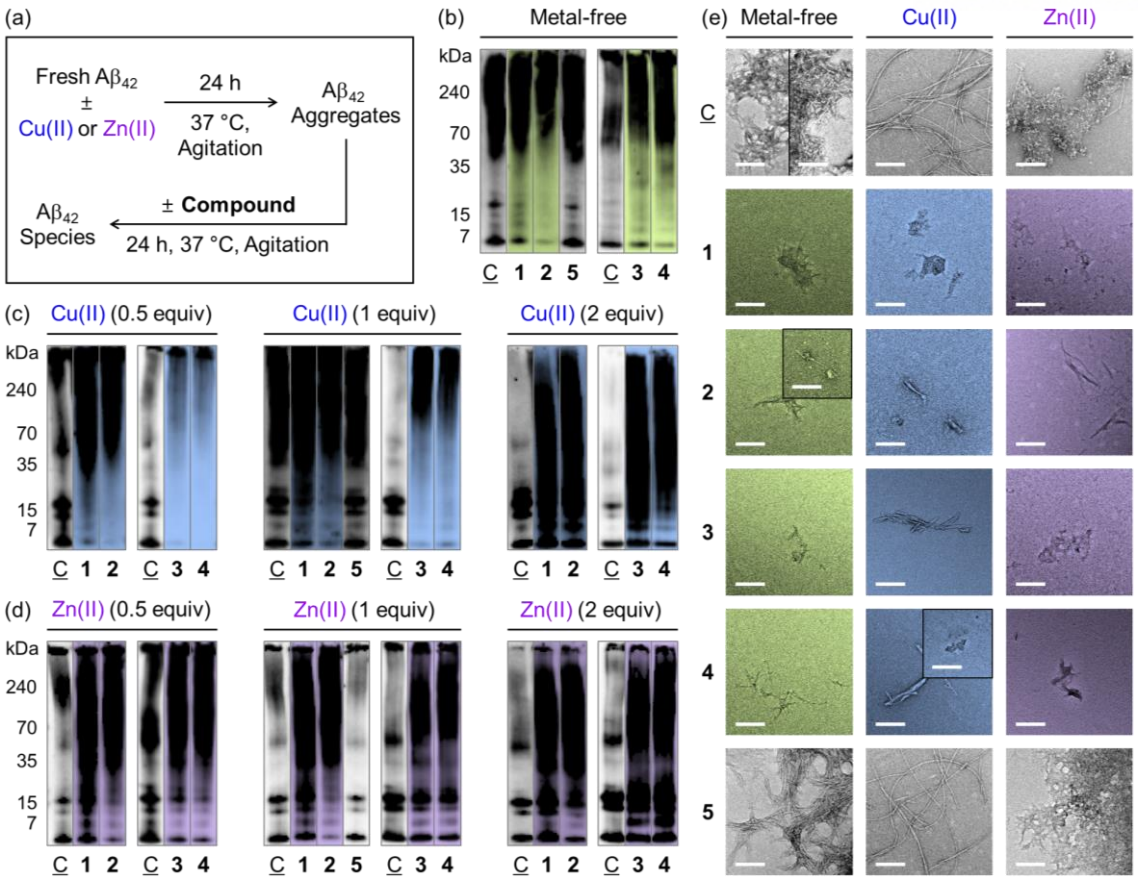

Figure 1.9. Influence of **1**–**5** on preformed metal-free or metal-induced Aβ$_{42}$ aggregates. (a) Scheme of the disaggregation experiments. (b-d) Gel/Western blots (6E10) of the Aβ$_{42}$ species generated in the (b) absence and (c and d) presence of metal ions. Lanes: (C) Aβ$_{42}$; (**1**) Aβ$_{42}$ + **1**; (**2**) Aβ$_{42}$ + **2**; (**3**) Aβ$_{42}$ + **3**; (**4**) Aβ$_{42}$ + **4**; (**5**) Aβ$_{42}$ + **5**. (e) TEM images of the samples obtained from (b) metal-free Aβ$_{42}$ and Aβ$_{42}$ with 1 equiv of (c) Cu(II) and (d) Zn(II). Conditions: [Aβ$_{42}$] = 25 μM; [Cu(II) or Zn(II)] = 12.5, 25, and 50 μM; [compound] = 50 μM; 20 mM HEPES, pH 7.4 [for metal-free or Zn(II)-containing samples] or pH 6.6 [for Cu(II)-added samples], 150 mM NaCl; 37 °C; 24 h; constant agitation. Scale bar = 200 nm.

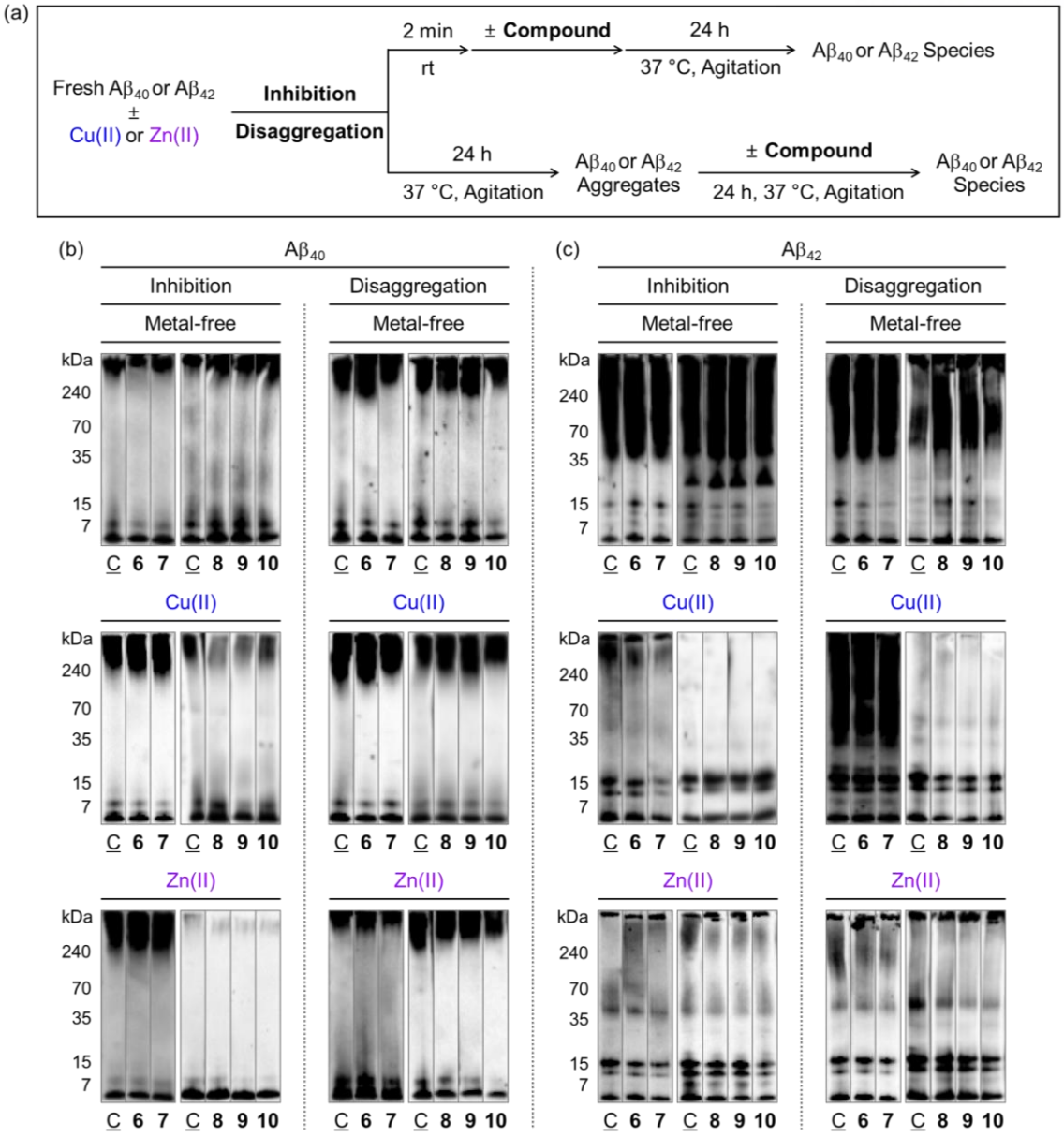

Figure 1.10. Effects of **6**–**10** on metal-free or metal-induced $A\beta_{40}$ and $A\beta_{42}$ aggregation pathways. (a) Scheme of the inhibition and disaggregation experiments. (b and c) Analysis of the resultant (b) $A\beta_{40}$ and (c) $A\beta_{42}$ species by gel/Western blot (6E10). Lanes: (C) $A\beta_{40/42}$; (**6**) $A\beta_{40/42}$ + **6**; (**7**) $A\beta_{40/42}$ + **7**; (**8**) $A\beta_{40/42}$ + **8**; (**9**) $A\beta_{40/42}$ + **9**; (**10**) $A\beta_{40/42}$ + **10**. Conditions: [$A\beta_{40/42}$] = 25 μM; [Cu(II) or Zn(II)] = 25 μM; [compound] = 50 μM; 20 mM HEPES, pH 7.4 [for metal-free or Zn(II)-containing samples] or pH 6.6 [for Cu(II)-added samples], 150 mM NaCl; 37 °C; 24 h; constant agitation.

The $A\beta_{40}$ disaggregation experiments (Figure 1.7) presented similar trends to those of the inhibition experiments. The compounds in **Group-I** altered the MW distribution of metal-free $A\beta_{40}$ and metal–$A\beta_{40}$ samples and their aggregate morphologies (Figure 1.7b-e), while the molecules in **Group-**

II did not exhibit such perceivable reactivity (Figures 1.7b-e and 1.10b). As depicted in Both inhibition and disaggregation experiments of $A\beta_{42}$ (Figures 1.8b-e, 1.9b-e, and 1.10c) indicated the similar results of the $A\beta_{40}$ studies. Our gel/Western blot and TEM data illustrated that the compounds in **Group-I**, designed to possess two electron-donating groups at the *p*-position on benzene, could modulate the formation of metal-free Aβ and metal–Aβ aggregates and disassemble the corresponding preformed aggregates. Furthermore, the contrasting lack of reactivity from the compounds in **Group-II**, embodying a less electron-dense benzene, implies a correlation between our molecules' oxidation potentials and their ability to interact with metal-free Aβ and metal–Aβ and redirect their aggregation pathways.

1.2.4. Oxidative Transformation of 1–10 in the Absence and Presence of Aβ and Metal Ions

To understand the distinction in the modulative reactivity of the molecules towards the aggregation of metal-free Aβ and metal–Aβ with respect to their redox properties, the chemical transformations of **Group-I** and **Group-II** were monitored in solution *via* UV–Vis spectroscopy under various conditions: with or without $A\beta_{40}$ in both the absence and presence of metal ions [*e.g.*, Cu(II) or Zn(II); Figures 1.11a and 1.12]. In the absence of $A\beta_{40}$ and metal ions, **1**'s optical spectrum exhibited an increase in absorption at *ca.* 530 nm resulting in the appearance of a broadband (Figure 1.12a, bottom), indicative of **1**'s transformation to an intermediate cationic radical and subsequent dimerization and trimerization of the cationic radicals.[57-59] The hypsochromic shift from *ca.* 300 to 250 nm implies the oxidative transformation of **1** to *p*-benzoquinonediimine (**BQDI**) or *p*-benzoquinone (**BQ**).[58,60] Addition of redox-active Cu(II) accelerated the oxidative transformation of **1**, reaching the maximum absorption in 4 h (at *ca.* 530 nm), while the introduction of Zn(II), a redox-inactive metal, did not noticeably alter the transformation kinetics (Figure 1.12a, bottom).

Notable optical changes of **1** were observed upon treatment of $A\beta_{40}$ with and without metal ions (Figures 1.11a and 1.12a, top). Under metal-free and Zn(II) conditions, absorbance at *ca.* 250 and 350 nm first gradually increased and decreased with time, respectively, indicating the transformation of **1** to **BQDI** or **BQ**.[58,60] The subsequent alterations of the peak intensity at *ca.* 250 nm (decrease) and *ca.* 350 nm (increase) denote **1**'s covalent interaction with $A\beta_{40}$.[32] In the presence of Cu(II) with $A\beta_{40}$, the optical spectra of **1** exhibited several distinct optical changes: (i) a significant sequential increase and decrease of the absorption band at *ca.* 250 nm; (ii) band intensification at *ca.* 350 nm, noticeably larger compared to those shown under metal-free and Zn(II)-present conditions; (iii) absence of the broad peak at *ca.* 500 nm, present under metal-free conditions, interpreted as a considerable decrease in the dimerization or trimerization of **1**, as a consequence of the fast and vigorous oxidation of **1** to **BQ** in the presence of Cu(II), followed by the covalent adduct formation of **BQ** with $A\beta_{40}$ species (Figure 1.11a, bottom).

In addition to **1**, the other compounds in **Group-II**, **2**–**4** were optically analyzed in the absence

and presence of $A\beta_{40}$ with or without metal ions. Under the absence of $A\beta_{40}$ conditions, the oxidative transformation of each compound was observed as previously reported (Figure 1.12b-d).[57,59,61-63] When the compounds were incubated with $A\beta_{40}$, the optical spectra showed that **2**–**4** were able to undergo oxidative transformation to **BQ** to form covalent bonds with $A\beta_{40}$, except for that of compound **3** due to substantial interference from **3**'s radical species (Figure 1.12b-d).[57,59,62] In contrast to the optical changes of the compounds in **Group-I**, the molecules in **Group-II** did not present perceivable spectral alterations throughout the measurement period under all conditions (Figure 1.12e-j). This bimodal trend suggests that a low oxidation potential is critical for undergoing the oxidative transformation of compounds to yield products (*i.e.*, **BQ**) capable of interacting with both metal-free Aβ and metal–Aβ. Collectively, our spectral data reveal the molecular mechanism conducive to the underlying interactions between **Group-I** and metal-free Aβ and metal–Aβ involving the oxidative transformation of the molecules.

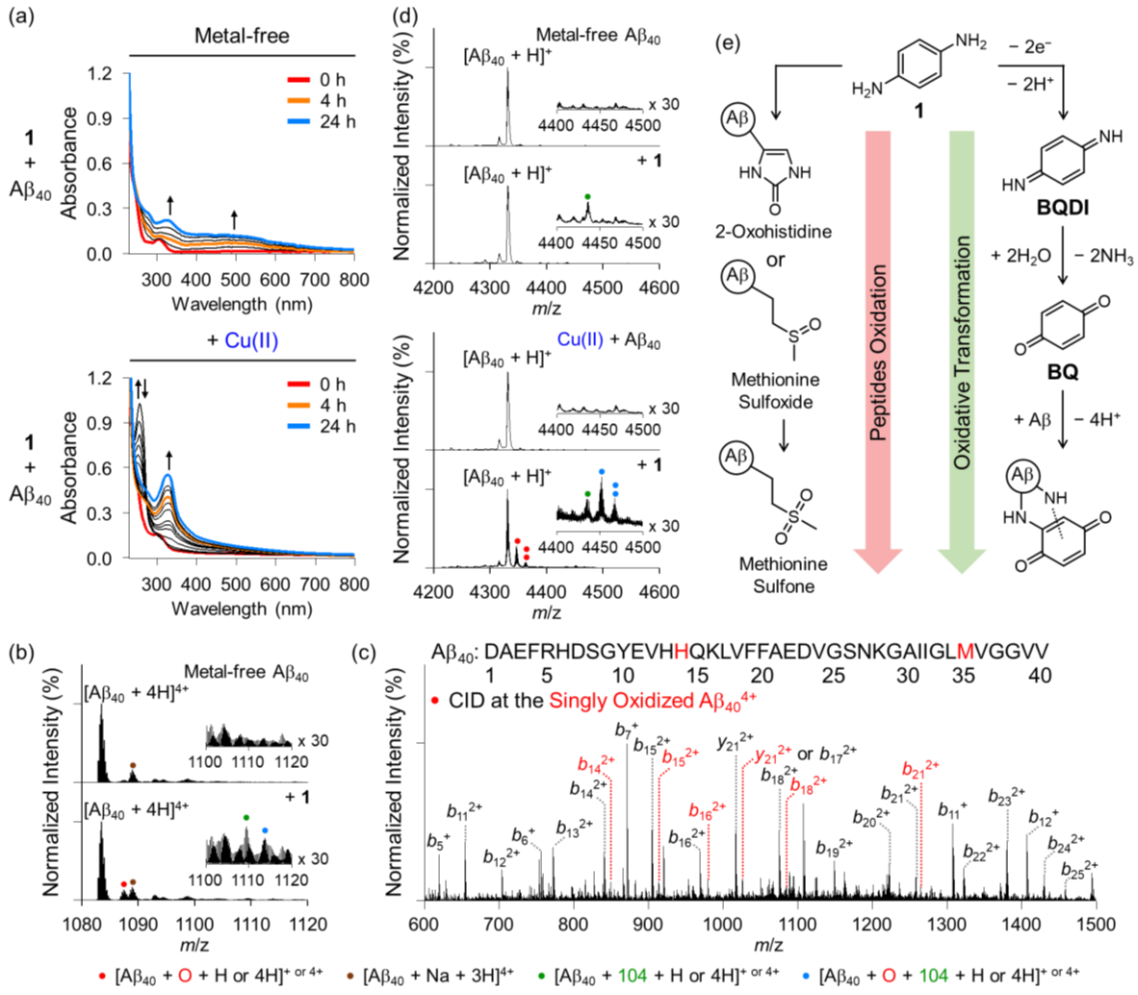

Figure 1.11. Analyses of **1**'s transformation and interaction with metal-free $A\beta_{40}$ or Cu(II)-associated $A\beta_{40}$ as well as proposed mechanisms. (a) Transfiguration of **1** in the presence of $A\beta_{40}$ with or without

Cu(II), detected by UV–Vis spectroscopy. Conditions: [$A\beta_{40}$] = 25 μM; [Cu(II)] = 25 μM; [**1**] = 50 μM; 20 mM HEPES, pH 7.4 (for metal-free samples) or pH 6.6 [for Cu(II)-added samples], 150 mM NaCl; 37 °C; 0-24 h; no agitation. (b-d) Interactions of **1** with metal-free $A\beta_{40}$ and Cu(II)-treated $A\beta_{40}$, analyzed by ESI–MS, ESI–MS^2, and MALDI–MS. $A\beta_{40}$ monomer incubated with **1** in the (b and d) absence and (d) presence of Cu(II) was detected by (b) ESI–MS or (d) MALDI–MS. Oxidized $A\beta_{40}$ and an adduct between $A\beta_{40}$ and oxidatively transformed **1** (*i.e.*, **BQ**) are indicated with red and blue circles, respectively. The covalent bond with $A\beta_{40}$ (green circle) was only observed from **1**-treated samples. (c) ESI–MS^2 spectrum of the singly oxidized $A\beta_{40}^{4+}$ produced upon addition of **1**. Conditions (for ESI–MS studies): [$A\beta_{40}$] = 50 μM; [**1**] = 100 μM; 1 mM ammonium acetate, pH 7.4; 37 °C; 24 h; no agitation. The samples were diluted by 10 fold with ddH_2O before injection to the mass spectrometer. Conditions (for MALDI–MS measurements): [$A\beta_{40}$] = 25 μM; [Cu(II)] = 25 μM; [**1**] = 50 μM; pH 7.4 (for metal-free samples) or pH 6.6 [for Cu(II)-added samples]; 37 °C; 24 h; constant agitation. (e) Two proposed pathways: (left) peptide oxidation by **1**; (right) Formation of a covalent adduct between Aβ and oxidatively transformed **1** (*i.e.*, **BQ**).

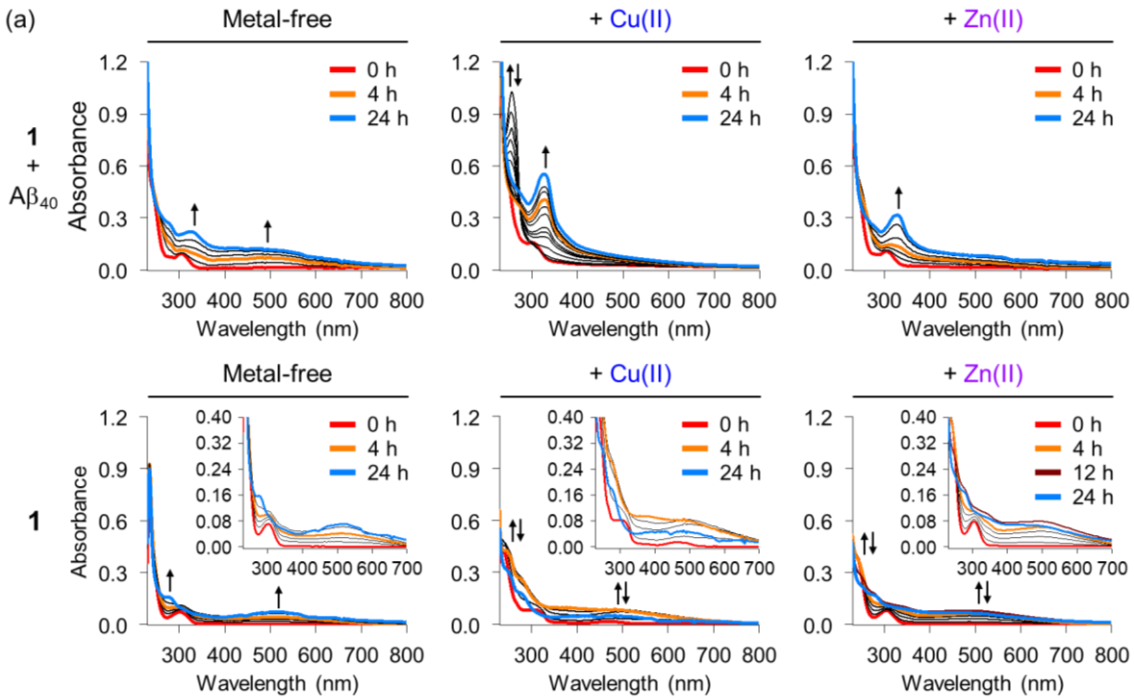

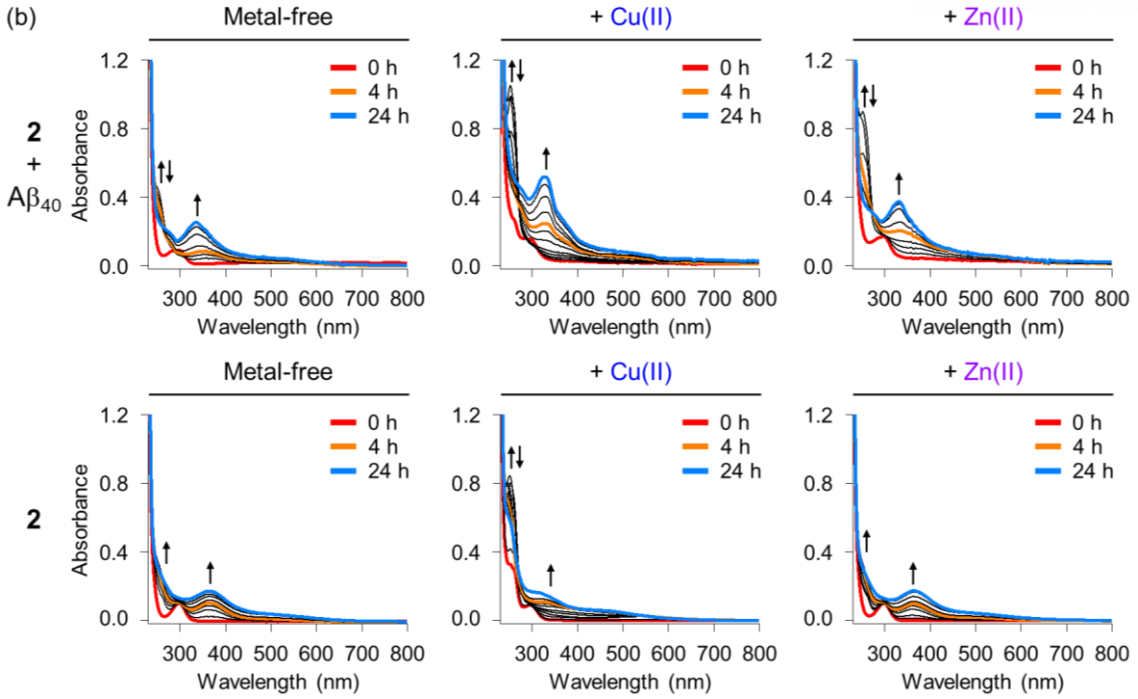

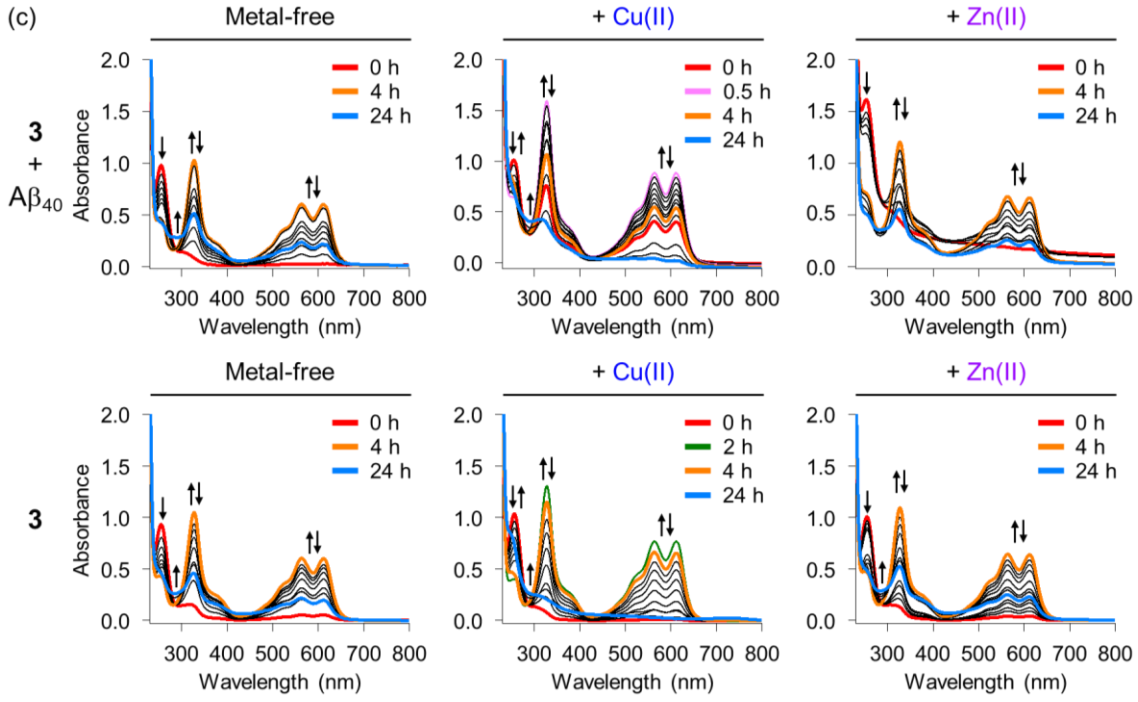

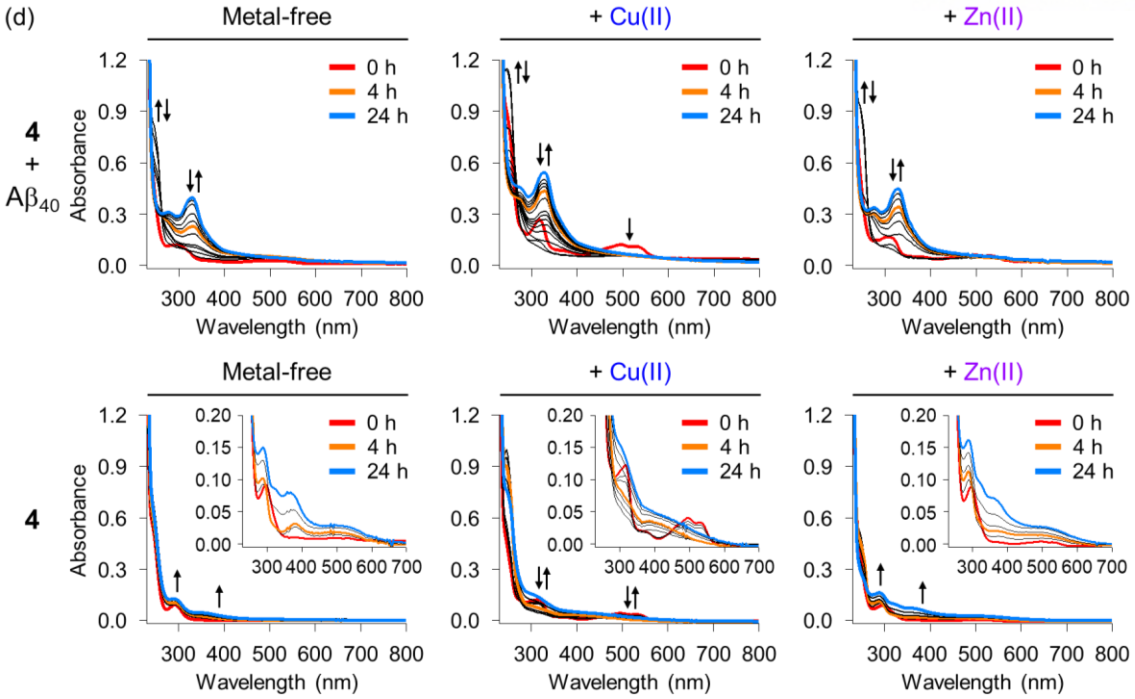

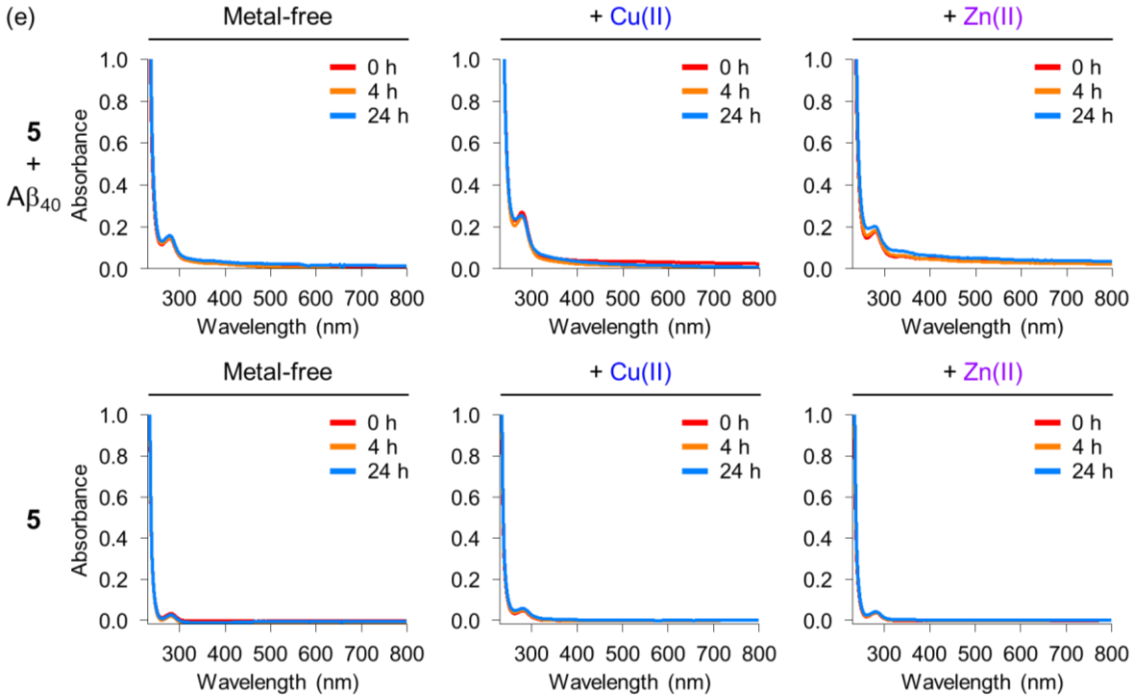

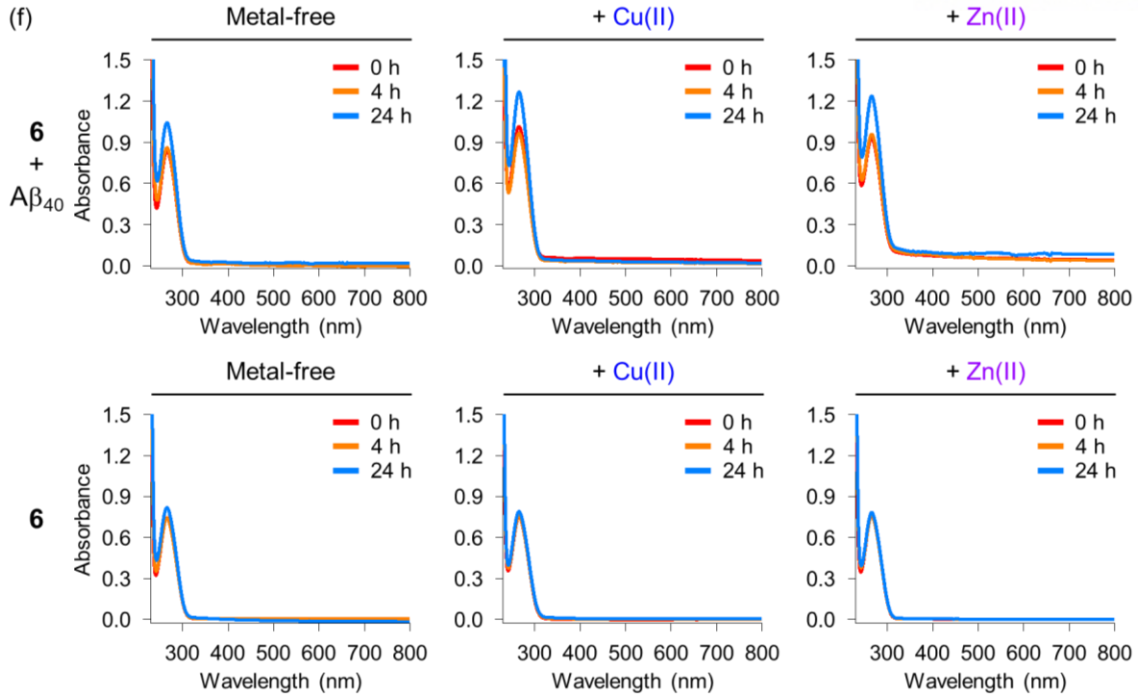

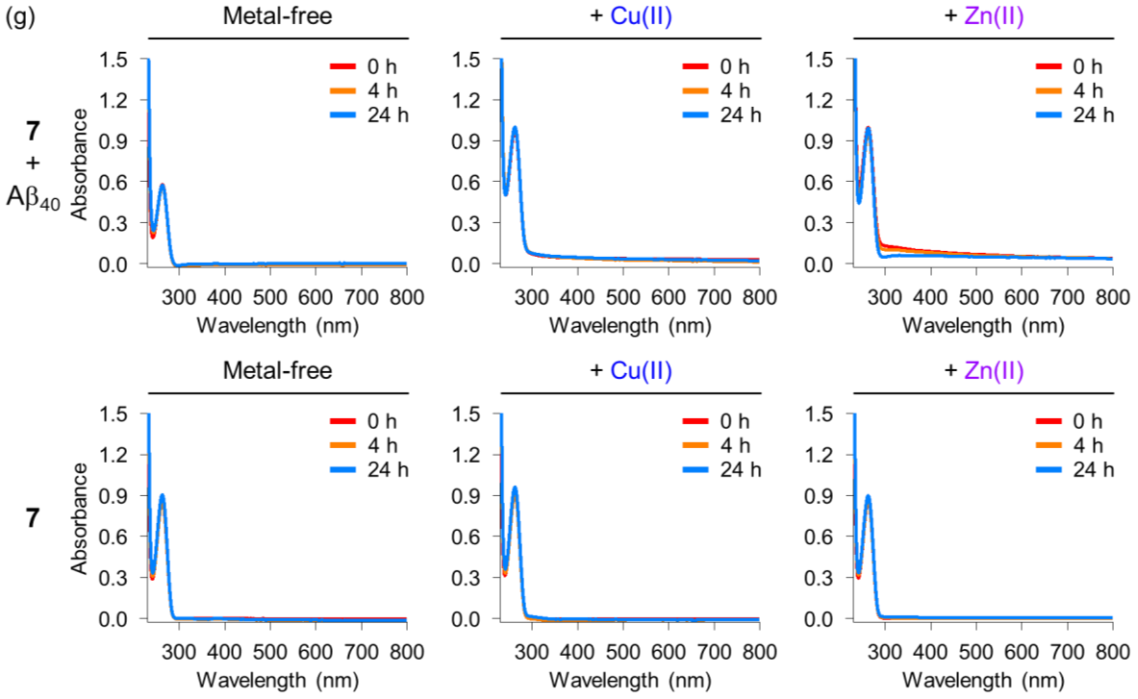

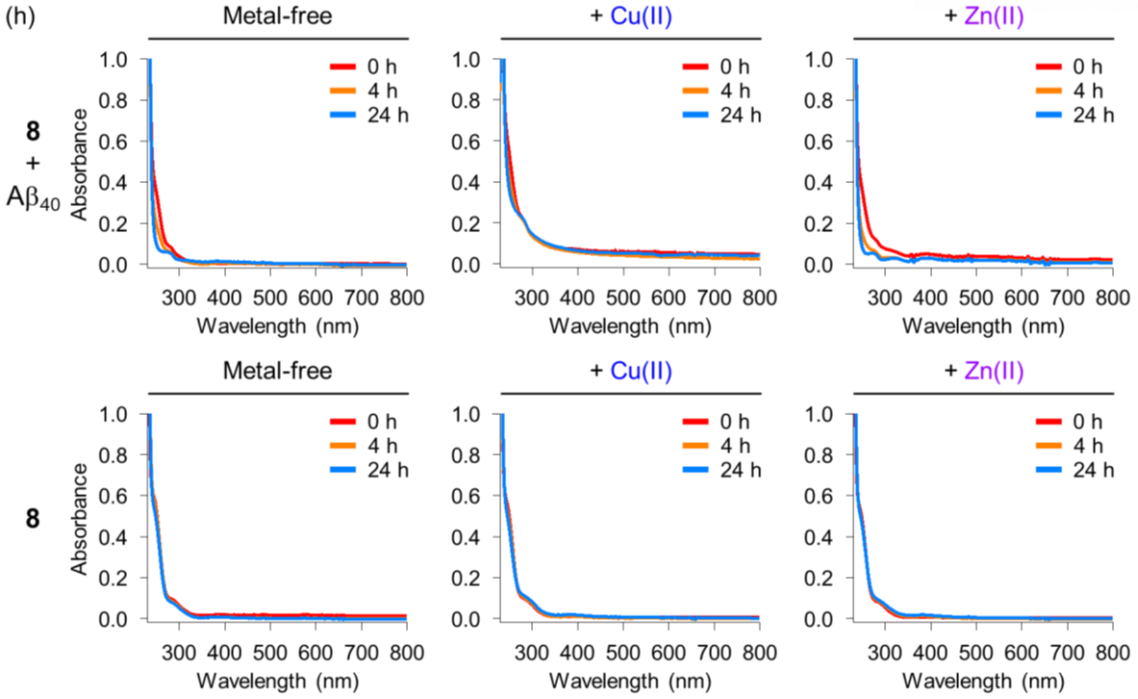

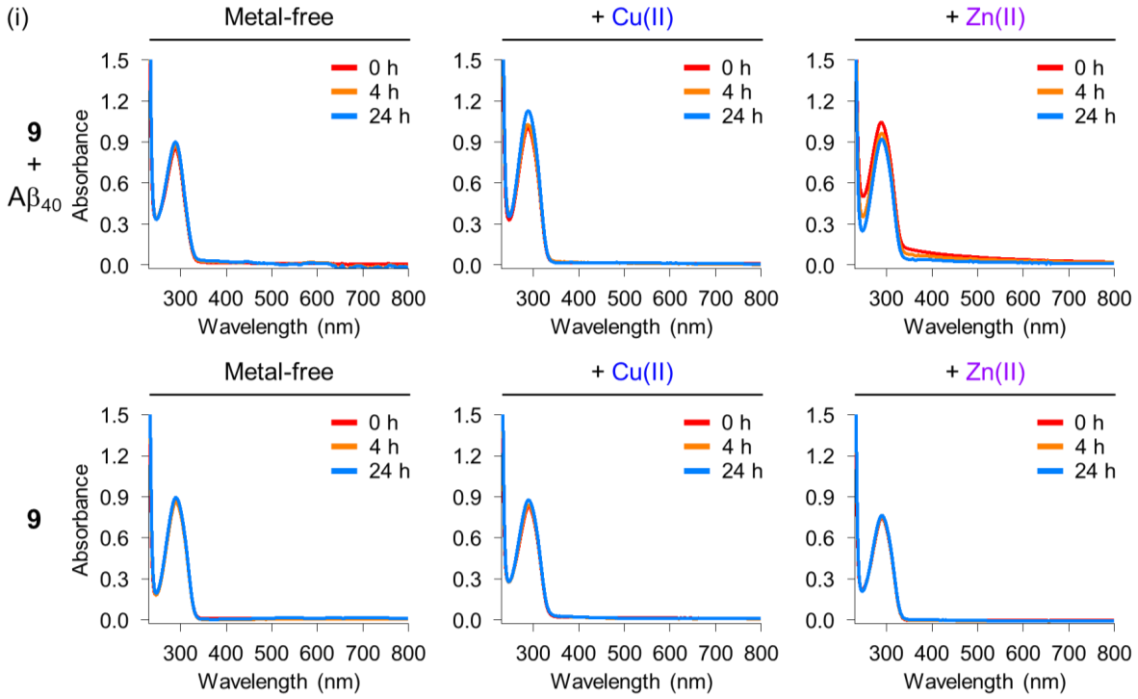

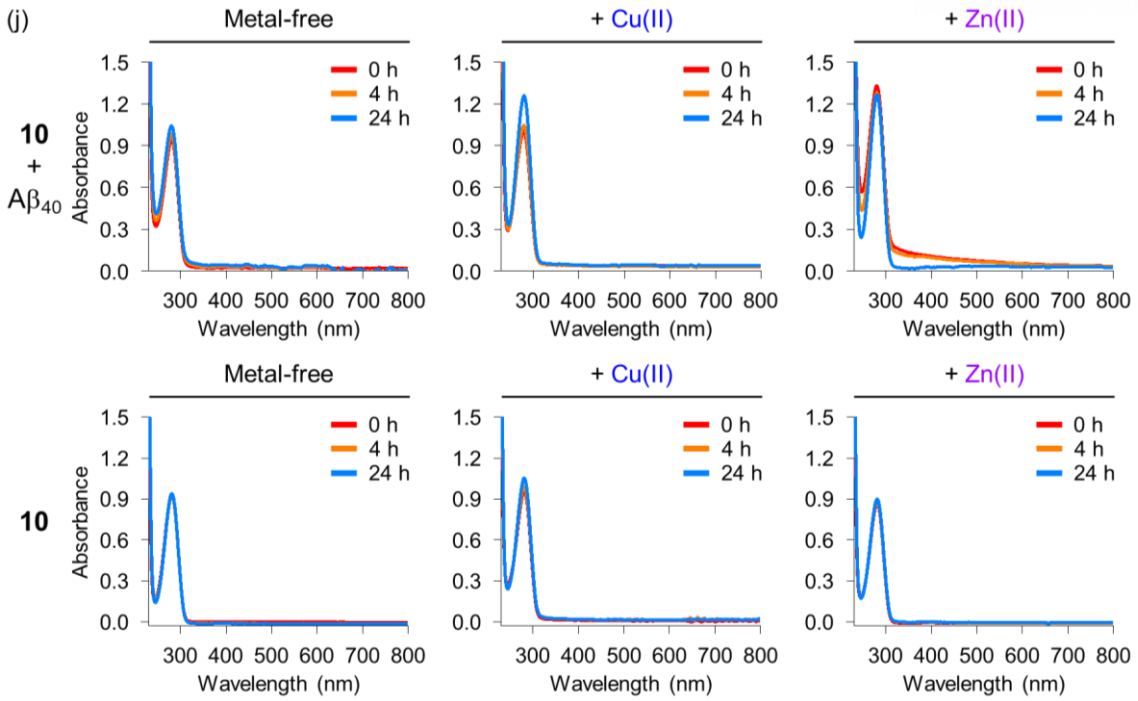

Figure 1.12. Transformation of **1**–**10** in the absence and presence of $A\beta_{40}$ with or without metal ions, detected by UV–Vis spectroscopy. Conditions: [$A\beta_{40}$] = 25 μM; [Cu(II) or Zn(II)] = 25 μM; [compound] = 50 μM; 20 mM HEPES, pH 7.4 [for metal-free or Zn(II)-containing samples] or pH 6.6 [for Cu(II)-added samples], 150 mM NaCl; 37 °C; 0-24 h; no agitation.

1.2.5. Interactions of 1–5 with Metal-free Aβ or Metal–Aβ

Predicted interactions between our compounds, **1**–**5**, and $A\beta_{40}$ were first visualized by employing a previously reported NMR structure of an $A\beta_{40}$ monomer (PDB 2LFM)[64] and AutoDoc Vina. Simulations showed that **1**–**5** were situated in a pocket near the self-recognition site (Figure 1.13a). The binding energy of these interaction was calculated to range from –4.7 to –4.0 kcal/mol (Figure 1.13b). Based on these results and referring back to our *in vitro* experiments (gel/Western blot and UV–Vis spectroscopy), in which only **1**–**4** exhibited the modulatory reactivity towards metal-free $A\beta_{40}$ aggregation, we propose that the redox potential of these compounds is a key factor for the capacity for interacting with Aβ and altering its aggregation pathways regardless of the regional interactions between the molecules and metal-free Aβ.

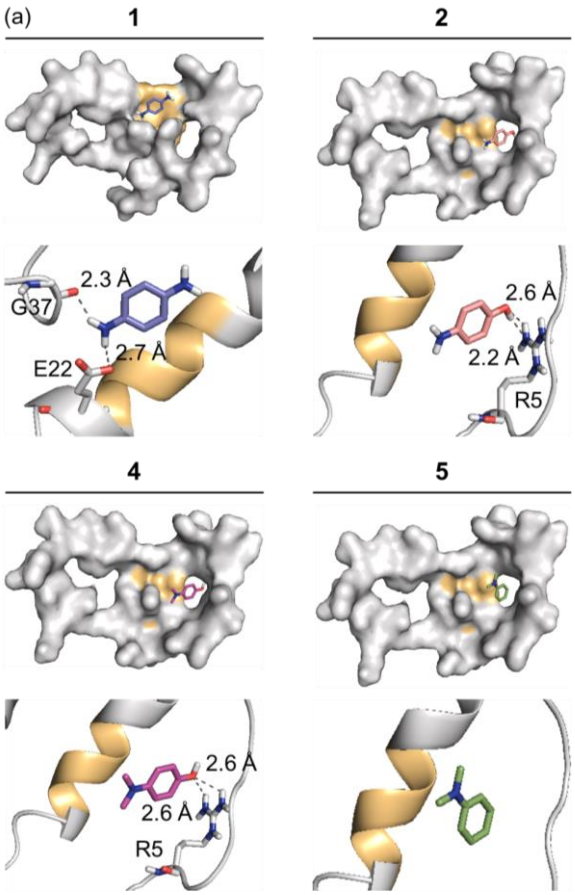

(b)

Cmpd	Binding Energy (kcal/mol)
1	−4.1
2	−4.1
3	−4.2
4	−4.7
5	−4.0

Figure 1.13. Docking studies of **1**–**5** with Aβ$_{40}$ monomer (PDB 2LFM). (a) Docked conformations of compounds with Aβ$_{40}$ (surface and zoon-in images). Hydrogen bonding between compounds and Aβ$_{40}$ is indicated with gray dashed lines (2.2-2.7 Å). The self-recognition site in Aβ$_{40}$ is highlighted in yellow. (b) Binding energy of the compounds with Aβ$_{40}$ monomer.

To identify the direct interactions between **1**–**5** and metal-free Aβ$_{40}$ or metal–Aβ$_{40}$ at the molecular level, two types of mass spectrometry [*i.e.*, electrospray ionization mass spectrometry (ESI–MS) and matrix-assisted laser desorption/ionization mass spectrometry (MALDI–MS)] were employed. ESI–MS studies were first conducted with the samples to verify the underlying mechanisms responsible for the modulating effects of **1**–**5** against metal-free Aβ$_{40}$ aggregation. The control experiments led to the detection of a peak at 1083 (or 1444) m/z corresponding to the +4 (or +3)-charged Aβ$_{40}$ monomer, respectively (Figures 1.11b and 1.14a). In the presence of the more redox-active molecules,**1**–**4** (**Group-I**), the addition of 104 Da to the +4 (or +3)-charged-Aβ$_{40}$ monomer [*i.e.*, covalent adduct formation with the transformed **1**–**4**, **BQ** (**BQ**–Aβ$_{40}$)[32]] was detected (green circles; Figures 1.11b and 1.14a).

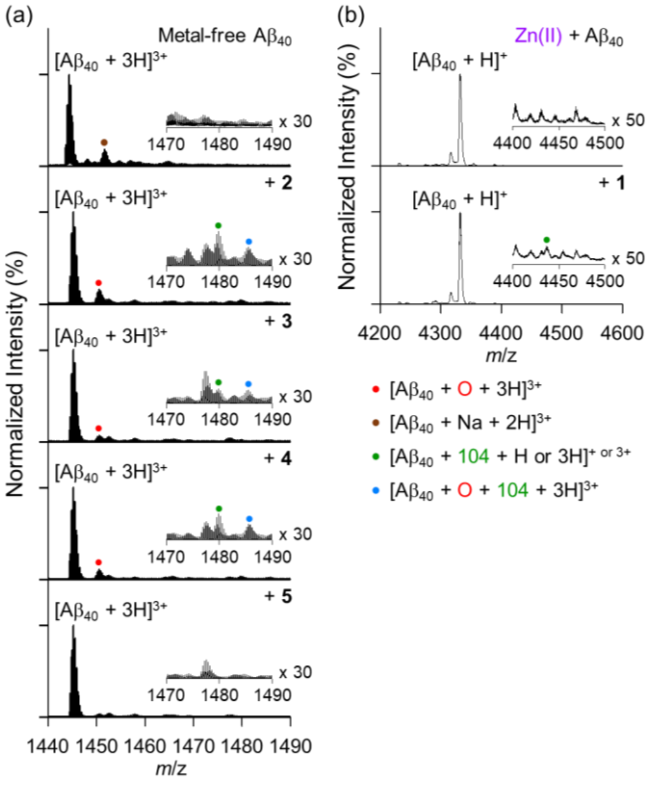

Figure 1.14. Interactions of **1**–**5** with metal-free and metal-treated $A\beta_{40}$. $A\beta_{40}$ monomer incubated (a) with **2**–**5** in the absence of metal ions and (b) with **1** in presence of Zn(II) was monitored by (a) ESI–MS and (b) MALDI–MS. Oxidized ions of $A\beta_{40}$ and $A\beta_{40}$–**BQ** adducts are indicated with red and blue circles, respectively. The covalent adducts between $A\beta_{40}$ and oxidatively transformed **1**–**4** (*i.e.*, **BQ**) are indicated with green circles. Conditions (for ESI–MS studies): [$A\beta_{40}$] = 50 μM; [compound] = 100 μM; 1 mM ammonium acetate, pH 7.4; 37 °C; 24 h; no agitation. The samples were diluted by 10 fold with ddH_2O before injection to the mass spectrometer. Conditions (for MALDI–MS measurements): [$A\beta_{40}$] = 25 μM; [Zn(II)] = 25 μM; [**1**] = 50 μM; pH 7.4; 37 °C; 24 h; constant agitation.

Peaks signifying the oxidation of $A\beta_{40}$, *ca.* 1087 m/z for $[A\beta_{40} + O + 4H]^{4+}$ or 1449 m/z for $[A\beta_{40} + O + 3H]^{3+}$, were also detected in the compound-treated samples of metal-free $A\beta_{40}$ (red circles; Figures 1.11b and 1.14a). Furthermore, new peaks (*ca.* 1113 $[A\beta_{40} + O + 104 + 4H]^{4+}$ or 1484 $[A\beta_{40} + O + 104 + 3H]^{3+}$ m/z), indicating the oxidized species of the covalent adduct (**BQ**–$A\beta_{40}$), were detected when metal-free $A\beta_{40}$ was treated with **Group-I** (blue circles; Figures 1.11b and 1.14a). Previous studies regarding the Aβ oxidation mechanism proposed that ROS, such as superoxide anion ($O_2^{\bullet-}$) or hydrogen peroxide (H_2O_2), possibly generated through the redox cycle[65] with **Group-I**, could oxidize Aβ and consequently modulate Aβ aggregation.[66-70] Tandem MS (ESI–MS^2) studies were carried out to determine the oxidation sites of the $[A\beta_{40} + O + 4H]^{4+}$ species (1087 m/z; red dot; Figure 1.11b) in the

presence of **1**, a representative of **Group-I**. Fragmental analysis of this peak, through collision-induced dissociation (CID), implicated His14 and Met35 as possible oxidation sites (Figure 1.11c), yielding 2-oxohistidine and methionine sulfoxide, respectively.[16,71] Interactions between **5** and $A\beta_{40}$ were identified as a representative study of **Group-II**, which did not exhibit significant reactivity towards metal-free Aβ and metal–Aβ in the experiments through gel/Western blot and UV–Vis spectroscopy (Figures 1.6-1.9, and 1.12e). Contrasting from the samples treated with the molecules in **Group-I**, ESI–MS analysis of the **5**-added $A\beta_{40}$ samples did not show the peaks corresponding to the covalent adduct with $A\beta_{40}$ or oxidized $A\beta_{40}$ (Figure 1.14a).

MALDI—MS was conducted to further investigate the interactions of **1** with metal-free $A\beta_{40}$ and metal–$A\beta_{40}$. Upon addition of **1** to the metal-free $A\beta_{40}$ samples, a new peak at 4436 m/z (*i.e.*, $[A\beta_{40} + 104 + H]^+$) was detected, indicative of a covalent adduct of the oxidatively transformed **1**, **BQ**, with the $A\beta_{40}$ monomer (Figure 1.11d). The covalent adduct formation was also detected in the presence of metal ions [*i.e.*, Cu(II) or Zn(II)] (Figures 1.11d and 1.14b). In the samples of Cu(II)–$A\beta_{40}$, new peaks corresponding to the addition of one or two oxygen atoms to $A\beta_{40}$ monomer (at 4348 and 4364 m/z) or **BQ**–$A\beta_{40}$ adducts (at 4452 and 4468 m/z) were observed, as in the ESI–MS analysis of the metal-free $A\beta_{40}$ samples incubated with **Group-I** (Figure 1.11d).

The presented MS data provide the mechanistic details of **Group-I**'s modulative reactivity towards the aggregation of both metal-free Aβ and metal–Aβ: covalent adduct formation and peptide oxidation. Both proposed mechanisms are strongly dependent on the redox properties of the molecules, since the oxidative transformation of **Group-I** is responsible for generating the covalent adducts (**BQ**) to Aβ and ROS (*e.g.*, $O_2^{\bullet-}$ and H_2O_2), as byproducts capable of inducing the oxidation of Aβ.[65,72] Together, our spectrometric observations support the significance of redox properties as a critical design parameter for molecules with multi-reactivity against metal-free Aβ and metal–Aβ. The distinct reactivities between **Group-I** and **Group-II**, observed *via* gel/Western blot, UV–Vis spectroscopy, and spectrometric studies, corroborate our redox-based design principle for multi-reactivity

1.2.6. Bioapplicability of 1–4

The bioapplicability (*e.g.*, cell viability, metabolic stability, and brain uptake) of **Group-I** was assessed prior to *in vivo* studies. First, cytotoxicity of **1**–**4** was determined in N2a cells through the MTT assay. N2a cells were treated with **1**–**4** at a range of concentrations (from 5 to 50 μM) for 24 h. Cells incubated with **1** showed *ca.* 80% viability at 50 μM. In contrast, cells exhibited *ca.* 70, 70, and 50% viability upon treatment with **2**, **3**, and **4**, respectively, at the same concentration (Figure 1.15). Second, the half-life ($t_{1/2}$) and intrinsic clearance (CI_{int}) of **1**–**4**, which are representative indicators for microsomal degradation of the molecules, were monitored as a measure of their metabolic stability. **1**, **2**, and **4** presented $t_{1/2}$ greater than 60 min and CI_{int} *ca.* 20 mL/min/mg, indicating their relatively metabolic

stability (Table 1.2). **3**, on the other hand, presented poor metabolic stability in comparison (74 mL/min/mg protein). Lastly, the blood-brain barrier (BBB) permeability of **1**, the least toxic and most metabolically stable candidate, was examined *in vivo*. Detection of **1** in the brains of CD1 mice, following oral administration (10 mg/kg), denoted the molecule's ability to cross the BBB (Table 1.3). Our evaluations of **Group-I**'s bioapplicability prompted **1** as a suitable candidate for further histochemical and behavioral *in vivo* investigations.

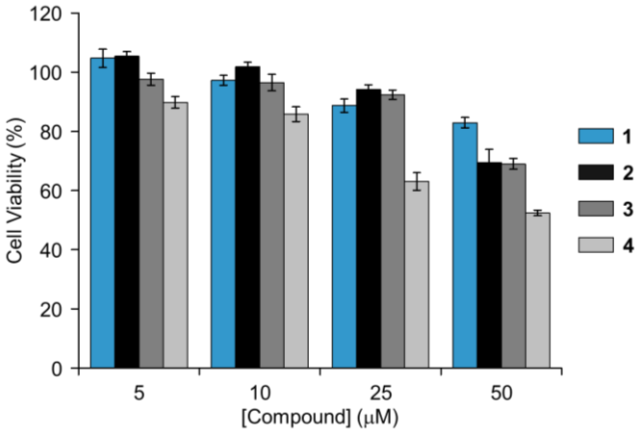

Figure 1.15. Cytotoxicity of **1**–**4**. Cell viability (%) of N2a cells incubated with various concentrations of **1**–**4** was obtained by the MTT assay. Error bars indicate the standard error from four independent experiments. Conditions: [compound] = 5, 10, 25, and 50 μM (1 % v/v DMSO); 37 °C; 24 h.

Table 1.2. Metabolic stability of **1**–**4**.

	$t_{1/2}$[a] (min)	Cl_{int}[b] (mL/min/mg Protein)
1	> 60	20
2	> 60	19
3	19	74
4	> 60	20

[a]Half-life ($t_{1/2}$); [b]intrinsic clearance (Cl_{int}).

Table 1.3. Concentrations of **1** in plasma, brain, and cerebrospinal fluid (CSF) after its 5 min administration in male CD1 mice [10 mg/kg; per os (*p.o.*) injection].

Matrix	Concentration (ng/mL or ng/g)[a]	SD[b]	CV (%)[c]
Plasma	1559	484	31.0
Brain	1676	437	26.1
CSF	3228	1849	57.3

[a]Mean (n = 3); [b]standard deviation; [c]coefficient of variation.

1.2.7. *In Vivo* Efficacies of 1 and BQ towards Aβ Accumulation and Cognitive Function in 5XFAD Mice

Based on its *in vitro* multi-reactivity and bioapplicability, **1** was selected as a representative molecule from **Group-I**, along with **BQ**, the final product of **1**'s oxidative transformation, as the chemical subjects of our *in vivo* studies regarding their *in vivo* efficacies in a transgenic AD murine model (*i.e.*, 5XFAD mice). 5XFAD is an AD transgenic mouse model overexpressing mutant human APP695 [Swedish (K670N/M671L), Florida (1716V), and London (V7171)] along with PS1 (M146L and L286V), inducing the rapid $A\beta_{42}$ production and onset of AD pathology.[32,33,73] First, the weight, physical appearance, and behavior of the mice were carefully examined every day for the duration of the compound administration. In comparison with the vehicle- and **1**-treated (1 mg/kg/day; *i.p.*) groups, which showed 0% (no death of 19 mice tested) and 14% (2 deaths of 14 mice) mortality, respectively, **BQ**-treated (1 mg/kg/day; *i.p.*) mice exhibited higher mortality rates (40%; 6 deaths of 15 mice). **BQ** treatment resulted in perceivable decreases (in males) and slight increases (in females) in weight among the survivors, whereas administration of vehicle and **1** yielded a general increase in weight (Table S4). Furthermore, **BQ**-treated 5XFAD mice manifested hypomotility and reduced task performance capacity relative to the vehicle- or **1**-treated 5XFAD mice (data not shown). Gross murine necropsy revealed the abnormal morphology of intraperitoneal organs including lesions at the injection site and severe internal adhesions accompanied by chronic inflammation in a majority of **BQ**-treated 5XFAD mice; such detriments were not observed in the vehicle- or **1**-treated mice (data not shown). Long-term *i.p.* administration of **BQ** induced significant toxicity in 5XFAD mice at 1 mg/kg/day and, at times, resulted in the termination of the test subject. In contrast, **1** (1 mg/kg/day) was sufficiently tolerated by 5XFAD mice throughout the repeated administration periods, reinforcing its *in vivo* safety.

Table 1.4. Change in the body weights of 5XFAD mice during the 30-repeated administrations of **1** and **BQ** [1 mg/kg/day; intraperitoneal (*i.p.*) injection].

Animal Group		Body Weight (g)		
Treatment	Sex	The Day of 1st Treatment	The Day of 30th Treatment	Gain
Vehicle	Male	26.2 ± 0.7 (10)[a]	26.8 ± 0.5 (10)	0.6
	Female	19.8 ± 0.6 (9)	22.4 ± 0.7 (9)	2.6
BQ	Male (*P* value *vs.* Vehicle)	25.5 ± 0.5 (8) (0.458)	24.7 ± 0.6 (4) (0.0400)	−0.8
	Female (*P* value *vs.* Vehicle)	19.5 ± 0.7 (7) (0.741)	20.3 ± 0.9 (5) (0.0876)	0.8
1	Male (*P* value *vs.* Vehicle)	26.8 ± 0.6 (7) (0.561)	27.7 ± 0.3 (6) (0.230)	0.9
	Female (*P* value *vs.* Vehicle)	19.8 ± 0.5 (7) (> 1.00)	23.5 ± 0.9 (6) (0.507)	3.7

[a]Mean ± s.e.m. (animal number).

Despite **BQ**'s prominent toxicity, the effects of **1** and **BQ** on amyloid deposition in the brains of 5XFAD mice were evaluated in the surviving population of test subjects (n = 12 of 14 mice and 9 of 15 mice for **1** and **BQ**, respectively). Enzyme-linked immunosorbent assay (ELISA) indicated the noticeable reduction in the levels of soluble [phosphate buffered saline (PBS)- and sodium dodecyl sulfate (SDS)-soluble fractions], insoluble [formic acid (FA)-soluble fractions], total (sum of PBS-, SDS-, and FA-soluble fractions) $A\beta_{42}$, and oligomeric Aβ species in the brains of **BQ**-treated 5XFAD mice, relative to those of vehicle-treated 5XFAD mice (20%, 7.4%, 15%, and 26% decrease, respectively); these differences, however, were not deemed statistically significant (Figure 1.16a). 4G8-immunohistochemical evaluations exhibited **BQ**-induced reduction in the levels of amyloid deposits (31%) with borderline statistical significance. Additionally, **BQ** was only able to decrease the deposition of compact congophilic amyloid plaques by 7.2% (Figure 1.16b,c). It should be noted that **BQ**'s toxicity likely poses a potential interference to the *in vivo* evaluation regarding the molecule's ability to curb the Aβ pathology in 5XFAD mice. Additional studies are warranted to elucidate the dose-dependent efficacy and toxicity of **BQ** and evaluate its effect on the behavior and cognitive function *in vivo* (Figure 1.17).

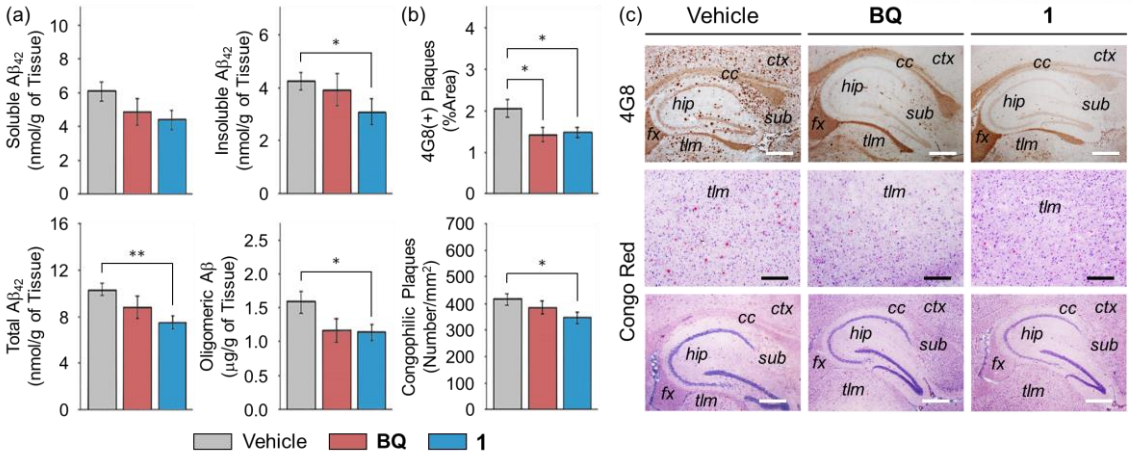

Figure 1.16. Analysis of the amounts of Aβ species in **1**- or **BQ**-treated 5XFAD mice. (a) Levels of soluble $A\beta_{42}$, insoluble $A\beta_{42}$, total $A\beta_{42}$, and oligomeric Aβ were analyzed in triplicate per sample by ELISA. Lanes: (Vehicle) 5XFAD + vehicle; (**BQ**) 5XFAD + **BQ**; (**1**) 5XFAD + **1**. (b) Loads of amyloid deposits and plaques in the brain expressed as the percent area of 4G8-immunoreactive deposits or the number of congophilic plaques per mm^2 of a region of interest, which was taken from hippocampal (*hip*), cortical (*ctx*) and thalamic (*tlm*) areas. (c) Representative images of 4G8-immunoreactive (1st row) or Congo red-positive (2nd and 3rd rows) amyloid deposits or plaques in *hip* and *ctx* (1st and 3rd rows), or *tlm* (2nd row) regions in the brains of vehicle- (1st column), **BQ**- (2nd column), or **1**-treated (3rd column) 5XFAD mice are shown. Congo red stained brain sections were also counter-stained with haematoxylin to differentiate the nuclei of neural cells (2nd and 3rd rows). Subiculum (*sub*), corpus callosum (*cc*), and fornix (*fx*). Scale bars = 500 μm (white) or 200 μm (black). The measurements were performed in five sagittal sections taken every 200 μm from midline per animal. Bars denote mean ± standard errors of mean (s.e.m.) (animal numbers; n = 19 for vehicle-treated 5XFAD mice; n = 9 for **BQ**-treated 5XFAD mice; n = 12 for **1**-treated 5XFAD mice). $^{*}P < 0.05$, or $^{**}P < 0.01$ by unpaired two-tail *t*-test.

In contract, **1** prominently attenuated the amyloid pathology in the brains of 5XFAD mice. All fractions of $A\beta_{42}$, analyzed (soluble, insoluble, and total $A\beta_{42}$) and oligomeric Aβ from the **1**-treated mice, were significantly reduced in comparison with the vehicle-treated 5XFAD mice (28%, 27%, 28%, and 28%, respectively; Figure 1.16a). **1** also diminished the deposition of 4G8-immunoreactive amyloid aggregates and compact congophilic amyloid plaques (28% and 17%, respectively; Figure 1.16b,c). Moreover, the repeated administration of **1** significantly improved the cognitive performance of 5XFAD mice. During the 5 day trial period of the Morris water maze (MWM) test, **1**-treated 5XFAD mice found the escape platform more easily and quickly relative to the vehicle- or **BQ**-treated 5XFAD mice (Figure 1.17a), showing that the treatment of **1** improved their spatial learning ability. In the subsequent probe test, which examines the long-term spatial memory of the mice, we found that **1**-treated 5XFAD mice

took shorter paths to the target zone (Figure 1.17b,c) and less time to reach the target location (Figure 1.17d), more frequently traversed the target location (Figure 1.17e), and spent more time in the target quadrant (Figure 1.17b,f). These results prove that **1** could effectively improve the spatial learning and memory of 5XFAD mice. Overall, our comparative *in vivo* evaluation of **1** and **BQ** demonstrate that although both molecules were able to reduce the cerebral and hippocampal Aβ load, **1** exhibited significantly lower toxicity and was much more efficient in reducing the Aβ pathology and recovering the cognitive ability in a transgenic AD model.

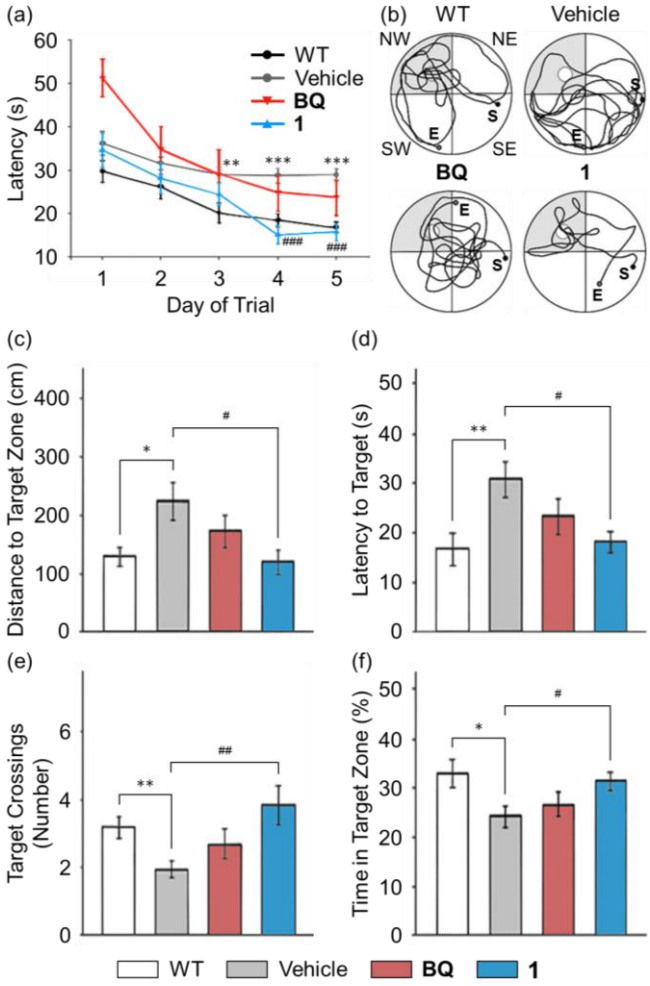

Figure 1.17. Measurement of spatial learning and memory improvements in **1**- or **BQ**-administrated 5XFAD mice. (a) Escape latency time daily assessed for five days from the day of the 30th compound treatment in the Morris water maze (MWM) test. From the 2nd training trial to the 5th trial, the latency time became significantly shorter in non-transgenic wild-type mice (WT; P = 0.012 by one-way ANOVA with Student-Newman-Keuls post hoc test) or **1**-treated 5XFAD mice (**1**; P = 0.0017), but not in vehicle- (Vehicle; P = 0.054) or **BQ**-treated (**BQ**; P = 0.40) 5XFAD mice. (b) After the MWM test, the probe trials were performed in the same water pool in the absence of the scape platform. All images

present the representative paths of the mice to search for the previous platform location [the small circle area in the gray, northwest (NW) target quadrant] for 60 s (from point S to point E). (c-f) In the probe test, we recorded (c) the path distance to first enter the target quadrant, (d) the latency time to touch the previous location of the platform, (e) the crossing frequency to traverse across the target platform, and (f) the times spent in the target quadrant to search for the platform. Lanes: (WT) wild-type; (Vehicle) 5XFAD + vehicle; (**BQ**) 5XFAD + **BQ**; (**1**) 5XFAD + **1**. The statistical comparisons were performed between vehicle-treated 5XFAD and their wild-type littermate mice (∗) or between vehicle- and **1**-treated 5XFAD mice (#). Bars denote mean ± s.e.m. (animal numbers; n = 17 for wild-type mice; n = 19 for vehicle-treated 5XFAD mice; n = 9 for **BQ**-treated 5XFAD mice; n = 12 for **1**-treated 5XFAD mice). $^{*,\#}P < 0.05$, $^{**,\#\#}P < 0.01$, or $^{***,\#\#\#}P < 0.001$ by unpaired two-tail *t*-test.

1.3. Conclusion

Difficulty in understanding the pathology of AD stems from its multifactorial nature. Ensuing inadequacy in comprehending the causes of neurodegeneration in AD severely impedes the development of therapeutics capable of halting the progression of the disease. To advance our understanding of AD pathology and discover effective therapeutics, small molecules capable of targeting multiple pathogenic factors have been designed as both investigative chemical tools and potential therapeutics. As a recently emerging concept, the structure-mechanism-based molecular design has presented the feasibility of controlling a molecule's reactivity towards various pathological factors of AD by tuning its electronic property. To consolidate this design strategy, we rationally devised compact molecules based on the simplest aromatic framework, benzene, by adjusting its electronic distribution to impart redox-dependent multi-reactivity against the pathological factors of AD (*i.e.*, free radicals, metal-free Aβ, and metal–Aβ). The molecules were classified into two groups: **Group-I** (**1**–**4**; incorporation of two electron-donating groups at the *p*-position onto benzene) and **Group-II** (**5**–**10**; containing an electron-donating group and additional structural modifications with electronic implications). Our biochemical and biophysical studies demonstrated the redox-dependent multi-reactivity of **Group-I** towards free radicals, metal-free Aβ, and metal–Aβ. Further spectroscopic and spectrometric results elucidated the mechanisms involved in the regulatory effects of **Group-I** against Aβ: covalent adduct formations and peptide oxidations. As a candidate molecule with favorable bioapplicability (*e.g.*, low cytotoxicity, moderate metabolic stability, and potential BBB permeability), **1** induced a significant reduction of cerebral and hippocampal Aβ deposits and produced statistically significant improvements in the cognitive function of 5XFAD mice. Taken together, our multidisciplinary studies establish and validate redox activity as a critical parameter to consider when designing compounds with multi-reactivity as observed through our redox-based design strategy of modifying the electronic properties of benzene. These studies can be helpful in understanding the uncovered relationships between the intertwined pathogenic factors and contribute towards efficiently

finding effective chemical reagents against AD.

1.4. Experimental Section

1.4.1. Materials and Methods

All chemical reagents were purchased from commercial suppliers and used as received unless otherwise stated. Benzene-1,4-diamine (**1**), 4-aminophenol (**2**), and 4-(dimethylamino)benzoic acid (**9**) were obtained from TCI (Chuo-ku, Tokyo, Japan). N^1,N^1,N^4,N^4-Tetramethylbenzene-1,4-diamine (**3**), aniline (**5**), 4-aminobenzoic acid (**6**), pyridin-4-amine (**7**), *N*,*N*-dimethylaniline (**8**), and *N*,*N*-dimethylpyridin-4-amine (**10**) were gained from Alfa Aesar (Ward Hill, MA, USA). 4-(Dimethylamino)phenol (**4**) was bought from Ark Pharm, Inc. (Arlington Heights, IL, USA). *p*-Benzoquinone (**BQ**) was gained from Sigma-Aldrich (St. Louis, MO, USA). $A\beta_{40}$ (DAEFRHDSGYEVHHQKLVFFAEDVGSNKGAIIGL-MVGGVV) and $A\beta_{42}$ (DAEFRHDSGYEV-HHQKLVFFAEDVGSNKGAIIGLMVGGVVIA) were purchased from Anaspec (Fremont, CA, USA). HEPES (2-[4-(2-hydroxyethyl)piperazin-1-yl]ethanesulfonic acid) was purchased from Sigma-Aldrich. The buffered solution was prepared in doubly distilled water [ddH_2O; a Milli-Q Direct 16 system (18.2 MΩ·cm; Merck KGaA, Darmstadt, Germany)]. Trace metal contamination was removed from the solutions used for the experiments by treating with Chelex (Sigma-Aldrich) overnight. Oxidation potentials of compounds were measured by a CHI620E potentiostat (CH Instruments, Inc., Bee Cave, TX, USA). Absorbance values obtained by the Trolox equivalent antioxidant capacity (TEAC) and MTT assays were determined by a SpectraMax M5e microplate reader (Molecular Devices, San Jose, CA, USA). Results obtained by gel electrophoresis with Western blotting (gel/Western blot) were visualized by a ChemiDoc MP imaging system (Bio-Rad, Hercules, CA, USA). Transmission Electron Microscopical images were acquired by a JEOL JEM-2100 transmission electron microscope [UNIST Central Research Facilities (UCRF), UNIST, Ulsan, Republic of Korea]. Docking studies of compounds with $A\beta_{40}$ monomer were carried out by AutoDock Vina 1.5.6 software. Optical spectra were recorded on an Agilent 8453 UV–Vis spectroscopy (Santa Clara, CA, USA). Mass spectra for examining the interactions of **1** and **3**–**5** with $A\beta_{40}$ in the absence and presence of Cu(II) or Zn(II) were taken on an Ultraflex III time-of-flight mass spectrometer (UCRF) or a Synapt G2-SI mass spectrometer [Daegu Gyeongbuk Institute of Science and Technology (DGIST) Center for Core Research Facilities (CCRF), DGIST, Daegu, Republic of Korea]. Metabolic stability to predict the half-life and clearance of compounds was evaluated with human liver microsomes [Daegu Gyeongbuk Medical Innovation Foundation (DGMIF), Daegu, Republic of Korea]. Analysis of the brain uptake of **1** in male CD1 mice was implemented at Shanghai ChemPartner (Shanghai, China).

1.4.2. Cyclic Voltammetry

Cyclic voltammograms were recorded under N_2 (g) with a CHI620E potentiostat (CH Instruments, Inc.)

and three electrodes composed of a glassy carbon working electrode (ALS Co., Ltd, Tokyo, Japan), an Ag/Ag(I) reference electrode (RE-7 non-aqueous reference electrode; ALS Co., Ltd), and a Pt wire auxiliary electrode (ALS Co., Ltd). Oxidation potentials of compounds (dissolved in DMSO; final concentration of 1 mM) were recorded in DMSO containing tetrabutylammonium hexafluorophosphate ($TBAPF_6$; 0.1 M) with the Ag/Ag(I) reference filled with the mixture (0.1 M $TBAPF_6$ and 0.01 M $AgNO_3$) at various scan rates (25, 50, 100, 150, 200, and 250 mV/s) at room temperature.

1.4.3. Trolox Equivalent Antioxidant Capacity (TEAC) Assay

The TEAC assay employing lysates of murine neuroblastoma Neuro-2a (N2a) cells [American Type Cell Collection (ATCC), Manassas, VA, USA] was conducted following the previously reported methods.[30,47] Cell lysates were prepared following a previously reported procedure with modifications.[74] The N2a cells were seeded in a six-well plate and grown to approximately 80-90% confluence. Cells were washed once with cold phosphate buffered saline (PBS, pH 7.4; GIBCO, Grand Island, NY, USA) and harvested by gently pipetting off adherent cells with cold PBS. The cell pellet was generated by centrifugation (2,000 *g* for 10 min at 4 °C) and sonicated on ice (5 s pulses, three times with 20 s intervals between each pulse) in 2 mL of cold buffer (5 mM potassium phosphate, pH 7.4, containing 0.9% NaCl and 0.1% glucose). The cell lysates were centrifuged at 5,000 *g* for 10 min at 4 °C. The supernatant was removed and stored on ice until use. To prepare the standard and samples in 96 well plates, 10 μL of the supernatant of cell lysates was delivered followed by the addition of metmyoglobin (10 μL, 55 μM; Sigma-Aldrich), 2,2'-azino-bis(3-ethylbenzthiazoline-6-sulphonic acid) (ABTS; 150 μL, 220 μM; Sigma-Aldrich), compound (10 μL), and H_2O_2 (40 μL, 412 μM) in order. Compounds concentration ranges utilized were as follows: Trolox, **1** and **2** (45, 90, 135, 180, 225, and 330 μM); **4** (50, 100, 150, 200, 250, and 300 μM); **3** (20, 40, 60, 80, 100, 120, and 140 μM). The absorbance values were recorded at 750 nm. The percent inhibition was calculated according to the measured absorbance [% inhibition = 100 x $(A_0 – A)/A_0$, where A and A_0 are the absorbance of the supernatant of cell lysates with and without compounds treatment, respectively] and was plotted as a function of a compound concentration. The TEAC values of compounds for each time point were calculated as a ratio of the slope of a compound to that of Trolox. The measurements were conducted in quadruplicate.

1.4.4. Aβ Aggregation Experiments

Aβ was dissolved in ammonium hydroxide [NH_4OH (aq), 1% v/v]. The resulting solution was aliquoted, lyophilized overnight, and stored at –80 °C. A stock solution of Aβ was then prepared by dissolving the lyophilized peptide using NH_4OH (aq) (10 μL, 1% v/v) and diluting with ddH_2O. All Aβ samples were prepared following the previously reported procedures.[30,32,75,76] The concentration of the peptide solution was determined by measuring the absorbance of the solution at 280 nm (ε = 1,450 $M^{-1}cm^{-1}$ for

$A\beta_{40}$; ε = 1,490 $M^{-1}cm^{-1}$ for $A\beta_{42}$). The buffered solution (20 mM HEPES, pH 7.4, 150 mM NaCl) was used for the preparation of Aβ samples. For the inhibition studies, compounds (final concentration, 50 μM; 1% v/v DMSO) were added to the samples of Aβ (25 μM) in the absence and presence of metal ions [Cu(II) or Zn(II); 25 μM] followed by incubation for 24 h at 37 °C with constant agitation. For the disaggregation studies, Aβ (25 μM) was incubated with and without metal ions [Cu(II) or Zn(II); 25 μM] for 24 h at 37 °C with constant agitation to generate preformed Aβ aggregates. The resulting Aβ aggregates were then treated with compounds (50 μM) and incubated for an additional 24 h with constant agitation.

1.4.5. Gel Electrophoresis with Western Blotting (Gel/Western blot)

The resultant Aβ species from *in vitro* experiments were analyzed through gel/Western blot using an anti-Aβ antibody (6E10).[30,32,75,76] The samples (10 μL) were separated on a 10-20% Tris-tricine gel (Invitrogen, Carlsbad, CA, USA). Following separation, the proteins were transferred onto nitrocellulose membranes and blocked with bovine serum albumin (BSA; 3% w/v; Sigma-Aldrich) in Tris-buffered saline (TBS) containing 0.1% Tween-20 (Sigma-Aldrich) (TBS-T) for 4 h at room temperature or overnight at 4 °C. The membranes were incubated with 6E10 (1:2,000, Covance, Princeton, NJ, USA) in a solution of BSA (2% w/v in TBS-T) for 2 h at room temperature or overnight at 4 °C. After washing with TBS-T (three times, 10 min), a horseradish peroxidase-conjugated goat anti-mouse secondary antibody (1:5,000 in 2% w/v BSA in TBS-T; Cayman Chemical Company, Ann Arbor, MI, USA) was added for 2 h at room temperature. A homemade ECL kit[47,77,78] was used to visualize gel/Western blot data on a ChemiDoc MP Imaging System (Bio-Rad).

1.4.6. Transmission Electron Microscopy (TEM)

Samples for TEM were prepared following the previously reported methods.[30,32,47,75-77] Glow-discharged grids (Formvar/Carbon 300-mesh, Electron Microscopy Sciences, Hatfield, PA, USA) were treated with Aβ samples (5 μL, 25 μM) for 2 min at room temperature. Excess sample was removed using filter paper followed by washing twice with ddH_2O. Each grid, incubated with uranyl acetate (5 μL, 1% w/v ddH_2O) for 1 min, was blotted off and dried for 15 min at room temperature. Images for each sample were taken on a JEOL JEM-2100 transmission electron microscope (200 kV; 25,000x magnification; UCRF). For the TEM studies, we randomly picked the locations of samples on the grids for taking images and collected more than 25 images from each grid (sample).

1.4.7. UV–Vis Spectroscopy

Oxidative transformation of compounds in the absence and presence of $A\beta_{40}$ with or without metal ions [*e.g.*, Cu(II) or Zn(II)] was monitored for 24 h at 37 °C by UV–Vis spectroscopy. Compounds (50 μM;

1% v/v DMSO) were added into the buffer solution [20 mM HEPES, pH 7.4 [for metal-free or Zn(II)-containing samples] or pH 6.6 [for Cu(II)-added samples], 150 mM NaCl] with or without $A\beta_{40}$ (25 μM) and/or $CuCl_2$ or $ZnCl_2$ (25 μM).

1.4.8. Docking Studies

Flexible ligand docking studies using AutoDock Vina[79] for **1**–**5** were conducted against the $A\beta_{40}$ monomer previously determined by NMR [Protein Data Bank (PDB) 2LFM].[64] One conformation was selected from twenty conformations within the PDB file. The MMFF94 energy minimization in ChemBio3D Ultra 11.0 was used to optimize the structure of **1**–**5** for the docking studies. The structures of $A\beta_{40}$ with **1**–**5** were prepared in AutoDock Tools[80] and imported into PyRx, which was used to run AutoDock Vina.[73] The exhaustiveness for the docking runs was set at 1,024. Docked models of **1**–**5** with the $A\beta_{40}$ monomer were visualized using Pymol.

1.4.9. Electrospray Ionization–Mass Spectrometry (ESI–MS)

The ESI–MS experiments were performed following the previously reported methods.[47,77] $A\beta_{40}$ (50 μM) was incubated with compounds (100 μM; 1% v/v DMSO) in 1 mM ammonium acetate (pH 7.4) at 37 °C without agitation. The incubated samples were diluted by 10 fold with water and then injected into the mass spectrometer. The capillary voltage, sampling cone voltage, and source temperature were set to 2.8 kV, 40 V, and 40 °C, respectively. The backing pressure was adjusted to 3.37 mbar. Gas flows for the helium were set to 180 mL/min. Tandem MS (ESI–MS^2) analyses were additionally conducted on the singly oxidized metal-free $A\beta_{40}$ with **1**. ESI parameters and experimental conditions were the same as above. Collision-induced dissociation (CID) was carried out by applying the collision energy in the trap at 45 V and adjusting the low mass (LM) resolution to 4.7 or 10 depending on the samples. More than 200 spectra were obtained for each sample and averaged for the analyses.

1.4.10. Matrix-assisted Laser Desorption Ionization–Mass Spectrometry (MALDI–MS)

$A\beta_{40}$ (25 μM) samples incubated with **1** (50 μM; 1% v/v DMSO) and/or metal ions [Cu(II) or Zn(II); 25 μM] in the buffer solution [pH 7.4 for metal-free or Zn(II)-containing samples or pH 6.6 for Cu(II)-added samples] were incubated at 37 °C for 24 h with constant agitation. Incubated $A\beta_{40}$, matrix [α-cyano-4-hydroxy-cinnamic acid (5 mg/mL) dissolved in 40% CH_3CN and 2% CF_3COOH], and 50 μM of the internal standard were mixed in a ratio of 5:4:1 and loaded on the MALDI–MS target plate. After thoroughly drying the samples, MALDI–MS spectra were obtained using an Ultraflex III time-of-flight mass spectrometer (UCRF).

1.4.11. Cell Viability Studies

N2a cells were maintained in media containing 50% Dulbecco's Modified Eagle Medium (DMEM; GIBCO) and 50% Opti-Minimal Essential Medium (Opti-MEM; GIBCO), and supplemented with 5% (v/v) fetal bovine serum (FBS; Sigma-Aldrich), 1% (v/v) L-glutamine (GIBCO), 100 U/mL penicillin (GIBCO), and 100 mg/mL streptomycin (GIBCO). N2a cells were grown and maintained at 37 °C in a humidified atmosphere with 5% CO_2. Cell viability upon treatment with compounds was determined by the MTT assay. Cells were seeded in a 96-well plate (5,000 cells in 100 μL per well) and were treated with compounds (5, 10, 25, and 50 μM; 1% v/v final DMSO concentration). After 24 h incubation, MTT [25 μL; 5 mg/mL in PBS (pH 7.4)] was added to each well and the plate was incubated for 4 h at 37 °C. Formazan produced by cells was solubilized using an acidic solution of *N*,*N*-dimethylformamide (aq) (DMF; 50% v/v,) and sodium dodecyl sulfate (SDS; 20% w/v) overnight at room temperature in the dark. Absorbance was measured at 600 nm by a microplate reader. Cell viability was calculated relative to cells containing an equivalent amount of DMSO. The measurements were conducted in quadruplicate.

1.4.12. Metabolic Stability

Compounds (1 μM) were added into PBS (0.1 M, pH 7.4; Corning, NY, USA) containing human liver microsomes (0.5 mg/mL; Corning) and were incubated for 5 min at 37 °C. The dihydronicotinamide adenine dinucleotide phosphate (NADPH; Promega, Madison, WI, USA) regeneration system solution was introduced to the pre-incubated mixture and then incubated for 15, 30, and 60 min at 37 °C. To terminate the reaction, CH_3CN including chlorpropamide known as an internal standard was added. After centrifugation (14,000 rpm, 4 °C) for 5 min, the supernatant was injected into the LC-MS/MS system (DGMIF) for the analysis.

1.4.13. Brain Uptake Studies

After 5 min administration of **1** in male CD1 mice [10 mg/kg; per os (*p.o.*) injection], the mice were manually restrained. Blood was taken from the animals *via* retro-orbital puncture for semi-serial bleeding or cardiac puncture (under anesthesia with isoflurane) for terminal bleeding into K2EDTA tubes. Blood samples were put on the ice and centrifuged to obtain plasma samples (2,000 *g*, 5 min under 4 °C) within 15 minutes. The animal was euthanized with pure CO_2 inhalation. A mid line incision was made on the neck. The muscle under the skin was cut to expose the cisterna magna. The cisterna magna was penetrated with the sharp end of one capillary. The cerebrospinal fluid (CSF) would be sucked spontaneously into the capillary. After CSF collection, a mid-line incision was made in the animal's scalp and skin retracted. The skull overlying the brain was removed. The whole brain was collected, rinsed with cold saline, dried on filtrate paper, and weighed; snap frozen by placing into dry ice. The supernatant diluted with H_2O and CH_3OH of each sample (*i.e.*, plasma, brain, and CSF) was injected for LC-MS/MS analysis.

1.4.14. *In Vivo* Efficacies

All animal studies were conducted in accordance with the guidelines of the Asan Institute for Life Science for Laboratory Animal Care and Use (Asan Medical Center, Seoul, Republic of Korea). Animals were housed with free access to water and food on 12 h light/dark cycle. Our studies used 5XFAD mice, a transgenic animal model of Alzheimer's disease (AD) that expresses the Swedish/London/Florida mutations of the human amyloid precursor protein (hAPP) and the M146L/L286V mutations of the human presenilin-1 (PSEN1) and develops the early and robust AD pathology with the cognitive impairments.[73] We maintained the mice on a C57BL/6 x SJL hybrid background. *In vivo* efficacy studies were thoroughly performed as previously described.[32,33] In brief, we daily treated 5XFAD mice by intraperitoneal (*i.p.*) routes with **1**, **BQ** (1 mg/kg of body weight), or the vehicle (1% DMSO in 20 mM HEPES, pH 7.4, 150 mM NaCl) for 30 successive days starting at three months of age. From the day of the 30th compound treatments, all animals experienced the Morris water maze (MWM) test with three trials per a day for five days to learn the spatial cognitive performance. After the last MWM trials, they also performed the probe test at 3 h in the same water pool to recall the memory to search for the previous location of the removed target platform. Variable parameters of the animal cognitive performance were recorded and evaluated using the SMART video tracking system (Harvard Apparatus, Holliston, MA, USA). Immediately after the cognitive performance test, the right and left cerebral hemispheres were collected from the brains of sacrificed mice for biochemical and histological analysis, respectively. Sandwich enzyme-linked immunosorbent assay (ELISA) was conducted to quantify the levels of human $A\beta_{42}$ (Invitrogen) or oligomeric Aβ (oAβ; Biosensis, Thebarton, South Australia) in PBS-, SDS-, or formic acid (FA)-soluble fractions following the serial centrifugal fractionations of the right cerebral hemispheres. To measure the depositions of amyloid plaques, the sagittal brain sections, which were prepared from the left hemispheres at 12 μm thickness, were subjected to Aβ-specific immunohistochemistry and histological staining using the human Aβ (17-24)-specific antibody 4G8 (Covance) and Accustain Congo Red amyloid staining solution (Sigma-Aldrich), respectively. The immuno-reacted or Congo Red-stained sections were examined or photographed under a light microscope (Eclipse 80i; Nikon, Tokyo, Japan). The loads of amyloid deposits in the brain were expressed as the percent area of 4G8-immunoreactive deposits or the number of congophilic plaques per mm^2 of the brain regions of interest (R.O.I.). Values were expressed as mean ± standard errors of mean (s.e.m.). Statistical differences between groups were evaluated by unpaired *t*-test or one-way analysis of variance (ANOVA) with Student-Newman-Keuls post hoc test, and considered significant at $P < 0.05$.

1.5. Acknowledgments

This research is supported by the National Research Foundation of Korea (NRF) grant funded by the

Korean government [NRF-2016R1A5A1009405 and NRF2017R1A2B3002585 (to M.H.L); NRF-2015R1A2A1A15052049 (to J.-Y.L.)]; the Korea Advanced Institute of Science and Technology (KAIST) (M.H.L.). J.K. acknowledges the Global Ph.D. fellowship program for support through the NRF funded by the Ministry of Education (NRF-2015HIA2A1030823). We also thank the previous our lab member, Dr. Shin Jung Lee, for initial data and analysis of MALDI–MS.

1.6. References

1. Apel, K.; Hirt, H. *Annu. Rev. Plant Biol.* **2004**, *55*, 373-399.
2. Valko, M.; Leibfritz, D.; Moncol, J.; Cronin, M. T.; Mazur, M.; Telser, J. *Int. J. Biochem. Cell Biol.* **2007**, *39*, 44-84.
3. Barnham, K. J.; Masters, C. L.; Bush, A. I. *Nat. Rev. Drug Discov.* **2004**, *3*, 205-214.
4. Uttara, B.; Singh, A. V.; Zamboni, P.; Mahajan, R. T. *Curr. Neuropharmacol.* **2009**, *7*, 65-74.
5. Greenough, M. A.; Camakaris, J.; Bush, A. I. *Neurochem. Int.* **2013**, *62*, 540-555.
6. Kim, G. H.; Kim, J. E.; Rhie, S. J.; Yoon, S. *Exp. Neurobiol.* **2015**, *24*, 325-340.
7. Jenner, P.; Olanow, C. W. *Neurology* **1996**, *47*, S161-S170.
8. Evans, P. H. *Br. Med. Bull.* **1993**, *49*, 577-587.
9. Zhao, Y.; Zhao, B. *Oxid. Med. Cell Longev.* **2013**, *2013*, 316523.
10. Savelieff, M. G.; Nam, G.; Kang, J.; Lee, H. J.; Lee, M.; Lim, M. H. *Chem. Rev.* **2018**, Article ASAP.
11. Maynard, C. J.; Bush, A. I.; Masters, C. L.; Cappai, R.; Li, Q. X. *Int. J. Exp. Pathol.* **2005**, *86*, 147-159.
12. Martins, R. N.; Villemagne, V.; Sohrabi, H. R.; Chatterjee, P.; Shah, T. M.; Verdile, G.; Fraser, P.; Taddei, K.; Gupta, V. B.; Rainey-Smith, S. R.; Hone, E.; Pedrini, S.; Lim, W. L.; Martins, I.; Frost, S.; Gupta, S.; O'Bryant, S.; Rembach, A.; Ames, D.; Ellis, K.; Fuller, S. J.; Brown, B.; Gardener, S. L.; Fernando, B.; Bharadwaj, P.; Burnham, S.; Laws, S. M.; Barron, A. M.; Goozee, K.; Wahjoepramono, E. J.; Asih, P. R.; Doecke, J. D.; Salvado, O.; Bush, A. I.; Rowe, C. C.; Gandy, S. E.; Masters, C. L. *J. Alzheimers Dis.* **2018**, *62*, 965-992.
13. Mecocci, P.; Polidori, M. C. *Biochim. Biophys. Acta* **2012**, *1822*, 631-638.
14. Persson, T.; Popescu, B. O. *Oxid. Med. Cell Longev.* **2014**, *2014*, 427318.
15. Kepp, K. P. *Chem. Rev.* **2012**, *112*, 5193-5239.
16. Cheignon, C.; Tomas, M.; Bonnefont-Rousselot, D.; Faller, P.; Hureau, C.; Collin, F. *Redox Biol.* **2018**, *14*, 450-464.
17. Hardy, J.; Selkoe, D. J. *Science* **2002**, *297*, 353-356.
18. Jakob-Roetne, R.; Jacobsen, H. *Angew. Chem. Int. Ed. Engl.* **2009**, *48*, 3030-3059.
19. DeToma, A. S.; Salamekh, S.; Ramamoorthy, A.; Lim, M. H. *Chem. Soc. Rev.* **2012**, *41*, 608-621.

20. Savelieff, M. G.; Lee, S.; Liu, Y.; Lim, M. H. *ACS Chem. Biol.* **2013**, *8*, 856-865.
21. Barnham, K. J.; Bush, A. I. *Curr. Opin. Chem. Biol.* **2008**, *12*, 222-228.
22. Barnham, K. J.; Bush, A. I. *Chem. Soc. Rev.* **2014**, *43*, 6727-6749.
23. Li, F.; Calingasan, N. Y.; Yu, F.; Mauck, W. M.; Toidze, M.; Almeida, C. G.; Takahashi, R. H.; Carlson, G. A.; Flint Beal, M.; Lin, M. T.; Gouras, G. K. *J. Neurochem.* **2004**, *89*, 1308-1312.
24. Nishida, Y.; Yokota, T.; Takahashi, T.; Uchihara, T.; Jishage, K.; Mizusawa, H. *Biochem. Biophys. Res. Commun.* **2006**, *350*, 530-536.
25. Kadowaki, H.; Nishitoh, H.; Urano, F.; Sadamitsu, C.; Matsuzawa, A.; Takeda, K.; Masutani, H.; Yodoi, J.; Urano, Y.; Nagano, T.; Ichijo, H. *Cell Death Differ.* **2005**, *12*, 19-24.
26. Rauk, A. *Chem. Soc. Rev.* **2009**, *38*, 2698-2715.
27. Savelieff, M. G.; DeToma, A. S.; Derrick, J. S.; Lim, M. H. *Acc. Chem. Res.* **2014**, *47*, 2475-2482.
28. Lane, D. J. R.; Ayton, S.; Bush, A. I. *J. Alzheimers Dis.* **2018**, *64*, S379-S395.
29. Schugar, H.; Green, D. E.; Bowen, M. L.; Scott, L. E.; Storr, T.; Bohmerle, K.; Thomas, F.; Allen, D. D.; Lockman, P. R.; Merkel, M.; Thompson, K. H.; Orvig, C. *Angew. Chem. Int. Ed. Engl.* **2007**, *46*, 1716-1718.
30. Lee, S.; Zheng, X.; Krishnamoorthy, J.; Savelieff, M. G.; Park, H. M.; Brender, J. R.; Kim, J. H.; Derrick, J. S.; Kochi, A.; Lee, H. J.; Kim, C.; Ramamoorthy, A.; Bowers, M. T.; Lim, M. H. *J. Am. Chem. Soc.* **2014**, *136*, 299-310.
31. Derrick, J. S.; Lim, M. H. *ChemBioChem* **2015**, *16*, 887-898.
32. Derrick, J. S.; Kerr, R. A.; Nam, Y.; Oh, S. B.; Lee, H. J.; Earnest, K. G.; Suh, N.; Peck, K. L.; Ozbil, M.; Korshavn, K. J.; Ramamoorthy, A.; Prabhakar, R.; Merino, E. J.; Shearer, J.; Lee, J. Y.; Ruotolo, B. T.; Lim, M. H. *J. Am. Chem. Soc.* **2015**, *137*, 14785-14797.
33. Beck, M. W.; Derrick, J. S.; Kerr, R. A.; Oh, S. B.; Cho, W. J.; Lee, S. J.; Ji, Y.; Han, J.; Tehrani, Z. A.; Suh, N.; Kim, S.; Larsen, S. D.; Kim, K. S.; Lee, J. Y.; Ruotolo, B. T.; Lim, M. H. *Nat. Commun.* **2016**, *7*, 13115.
34. Han, J.; Lee, H. J.; Kim, K. Y.; Lee, S. J. C.; Suh, J. M.; Cho, J.; Chae, J.; Lim, M. H. *ACS. Chem. Neurosci.* **2018**, *9*, 800-808.
35. Beck, M. W.; Derrick, J. S.; Suh, J. M.; Kim, M.; Korshavn, K. J.; Kerr, R. A.; Cho, W. J.; Larsen, S. D.; Ruotolo, B. T.; Ramamoorthy, A.; Lim, M. H. *ChemMedChem* **2017**, *12*, 1828-1838.
36. Cooper, D. L.; Gerratt, J.; Raimondi, M. *Nature* **1986**, *323*, 699-701.
37. Pauling, L. *Nature* **1987**, *325*, 396-396.
38. Messmer, R. P.; Schultz, P. A. *Nature* **1987**, *329*, 492-492.
39. Politzer, P.; Abrahmsen, L.; Sjoberg, P. *J. Am. Chem. Soc.* **1984**, *106*, 855-860.
40. Mecozzi, S.; West, A. P., Jr.; Dougherty, D. A. *Proc. Natl. Acad. Sci. U. S. A.* **1996**, *93*, 10566-10571.

41. Pelzer, K. M.; Cheng, L.; Curtiss, L. A. *J. Phys. Chem. C* **2017**, *121*, 237-245.
42. Walter, R. I. *J. Am. Chem. Soc.* **1966**, *88*, 1923-1930.
43. Janzen, E. G. *Acc. Chem. Res.* **1969**, *2*, 279-288.
44. Re, R.; Pellegrini, N.; Proteggente, A.; Pannala, A.; Yang, M.; Rice-Evans, C. *Free Radic. Biol. Med.* **1999**, *26*, 1231-1237.
45. van den Berg, R.; Haenen, G. R. M. M.; van den Berg, H.; Bast, A. *Food Chem.* **1999**, *66*, 511-517.
46. Arts, M. J. T. J.; Sebastiaan Dallinga, J.; Voss, H.-P.; Haenen, G. R. M. M.; Bast, A. *Food Chem.* **2004**, *88*, 567-570.
47. Lee, H. J.; Korshavn, K. J.; Nam, Y.; Kang, J.; Paul, T. J.; Kerr, R. A.; Youn, I. S.; Ozbil, M.; Kim, K. S.; Ruotolo, B. T.; Prabhakar, R.; Ramamoorthy, A.; Lim, M. H. *Chem. Eur. J.* **2017**, *23*, 2706-2715.
48. Rao, P. S.; Hayon, E. *J. Phys. Chem.* **1975**, *79*, 1063-1066.
49. Benmehdi, H.; Behilil, A.; Memmou, F.; Amrouche, A. *Arab. J. Chem.* **2017**, *10*, S1402-S1408.
50. Lee, S. J.; Nam, E.; Lee, H. J.; Savelieff, M. G.; Lim, M. H. *Chem. Soc. Rev.* **2017**, *46*, 310-323.
51. Smith, D. P.; Ciccotosto, G. D.; Tew, D. J.; Fodero-Tavoletti, M. T.; Johanssen, T.; Masters, C. L.; Barnham, K. J.; Cappai, R. *Biochemistry* **2007**, *46*, 2881-2891.
52. Noy, D.; Solomonov, I.; Sinkevich, O.; Arad, T.; Kjaer, K.; Sagi, I. *J. Am. Chem. Soc.* **2008**, *130*, 1376-1383.
53. Tougu, V.; Karafin, A.; Zovo, K.; Chung, R. S.; Howells, C.; West, A. K.; Palumaa, P. *J. Neurochem.* **2009**, *110*, 1784-1795.
54. Pedersen, J. T.; Ostergaard, J.; Rozlosnik, N.; Gammelgaard, B.; Heegaard, N. H. *J. Biol. Chem.* **2011**, *286*, 26952-26963.
55. Felice, F. G. D.; Vieira, M. N. N.; Saraiva, L. M.; Figueroa-Villar, J. D.; Garcia-Abreu, J.; Liu, R.; Chang, L.; Klein, W. L.; Ferreira, S. T. *FASEB J.* **2004**, *18*, 1366-1372.
56. Meek, A. R.; Simms, G. A.; Weaver, D. F. *Can. J. Chem.* **2012**, *90*, 865-873.
57. Chung, Y.-C.; Su, Y. O. *J. Chin. Chem. Soc.* **2009**, *56*, 493-503.
58. Bai, Y.-H.; Li, J.-Y.; Zhu, Y.-h.; Xu, J.-J. *Electroanal.* **2010**, *22*, 1239-1247.
59. Lauw, S. J. L.; Xu, X.; Webster, R. D. *ChemPlusChem* **2015**, *80*, 1288-1297.
60. Meyer, A.; Fischer, K. *Environ. Sci. Eur.* **2015**, *27*, 11.
61. Lerner, L. *J. Phys. Chem. A* **2011**, *115*, 9901-9910.
62. Sumalekshmy, S.; Gopidas, K. R. *Chem. Phys. Lett.* **2005**, *413*, 294-299.
63. Eyer, P.; Lengfelder, E. *Biochem. Pharmacol.* **1984**, *33*, 1005-1013.
64. Vivekanandan, S.; Brender, J. R.; Lee, S. Y. *Biochem. Biophys. Res. Commun.* **2011**, *411*, 312-316.
65. Kappus, H.; Sies, H. *Experientia* **1981**, *37*, 1233-1241.

66. Watson, A. A.; Fairlie, D. P.; Craik, D. J. *Biochemistry* **1998**, *37*, 12700-12706.
67. Palmblad, M.; Westlind-Danielsson, A.; Bergquist, J. *J. Biol. Chem.* **2002**, *277*, 19506-19510.
68. Hou, L.; Kang, I.; Marchant, R. E.; Zagorski, M. G. *J. Biol. Chem.* **2002**, *277*, 40173-40176.
69. Hou, L.; Shao, H.; Zhang, Y.; Li, H.; Menon, N. K.; Neuhaus, E. B.; Brewer, J. M.; Byeon, I. J.; Ray, D. G.; Vitek, M. P.; Iwashita, T.; Makula, R. A.; Przybyla, A. B.; Zagorski, M. G. *J. Am. Chem. Soc.* **2004**, *126*, 1992-2005.
70. Kang, J.; Lee, S. J.; Nam, J. S.; Lee, H. J.; Kang, M. G.; Korshavn, K. J.; Kim, H. T.; Cho, J.; Ramamoorthy, A.; Rhee, H. W.; Kwon, T. H.; Lim, M. H. *Chem. Eur. J.* **2017**, *23*, 1645-1653.
71. Vogt, W. *Free Radic. Biol. Med.* **1995**, *18*, 93-105.
72. Stadtman, E. R.; Levine, R. L. *Amino Acids* **2003**, *25*, 207-218.
73. Oakley, H.; Cole, S. L.; Logan, S.; Maus, E.; Shao, P.; Craft, J.; Guillozet-Bongaarts, A.; Ohno, M.; Disterhoft, J.; Van Eldik, L.; Berry, R.; Vassar, R. *J Neurosci* **2006**, *26*, 10129-10140.
74. Spencer, V. A.; Sun, J. M.; Li, L.; Davie, J. R. *Methods* **2003**, *31*, 67-75.
75. Choi, J. S.; Braymer, J. J.; Nanga, R. P.; Ramamoorthy, A.; Lim, M. H. *Proc. Natl. Acad. Sci. U. S. A.* **2010**, *107*, 21990-21995.
76. Hindo, S. S.; Mancino, A. M.; Braymer, J. J.; Liu, Y.; Vivekanandan, S.; Ramamoorthy, A.; Lim, M. H. *J. Am. Chem. Soc.* **2009**, *131*, 16663-16665.
77. Beck, M. W.; Oh, S. B.; Kerr, R. A.; Lee, H. J.; Kim, S. H.; Kim, S.; Jang, M.; Ruotolo, B. T.; Lee, J. Y.; Lim, M. H. *Chem. Sci.* **2015**, *6*, 1879-1886.
78. Mruk, D. D.; Cheng, C. Y. *Spermatogenesis* **2011**, *1*, 121-122.
79. Trott, O.; Olson, A. J. *J. Comput. Chem.* **2010**, *31*, 455-461.
80. Morris, G. M.; Huey, R.; Lindstrom, W.; Sanner, M. F.; Belew, R. K.; Goodsell, D. S.; Olson, A. J. *J. Comput. Chem.* **2009**, *30*, 2785-2791.

Chapter 2.

Detection of Metal Ions by Fluorescent Probes in Living Cells

The results, presented in this Chapter, were published or submitted: (1) Yun, J. Y.; Chae, J. B.; Kim, M.; Lim, M. H.; Kim, C. *Photochem. Photobiol. Sci.* **2019**, Accepted for Publication; (2) Kim, M. S.; Yun, D.; Lee, H.; Kim, M.; Lim, M. H.; Kim, C.; Kim, K.-T. Submitted for Publication; (3) Yun, D.; Kang, J. H.; Kim, M. S.; Kim, M.; Lim, M. H.; Kim, C. Submitted for Publication. I conducted the live-cell imaging experiments using the newly developed sensors for detection of metal ions in living cells.

2.1. Introduction

Zn^{2+} plays a key role in biological systems, such as apoptosis and signal transduction.[1-5] Dyshomeostasis of Zn^{2+}, however, has been suggested as a pathological feature in neurodegenerative diseases [*e.g.*, Alzheimer's disease (AD), Parkinson's disease, and amyotrophic lateral sclerosis].[1-5] In addition to Zn^{2+}, the absorption and accumulation of Al^{3+} in the brain, taken from the environment, diet, and medication, has been also reported to be implicated in the pathology of AD.[4,6,7] In order to further advance our understanding of how abnormal levels and control of metals could affect the pathogenesis of AD, visualization of Zn^{2+} and Al^{3+} in the brain would help understand their involvement in the disease. Thus, as an efficient and effective method, fluorescent imaging to identify the location of metals, utilizing a fluorescence-based probe, has been conducted.[5,8] In this Chapter, the utilization of the newly synthesized three chemosensors for detecting Zn^{2+} and Al^{3+} in living cells is described.

2.2. Results and Discussion

2.2.1. Turn-on Fluorescent Probe, DHIC, for Zn^{2+} in Living Cells

To monitor Zn^{2+} in biological systems, **DHIC** was synthesized through the condensation reaction of imidazole with a water-soluble 4-(diethylamino)salicylaldehyde moiety.[9] **DHIC** (20 μM) was pre-incubated in living cells for 1 h prior to incubation with Zn^{2+} (600 μM) for 1 h. The fluorescent response of **DHIC** to Zn^{2+} was monitored at the green fluorescence protein (GFP) channel [λ_{ex} = 470 (± 11) nm; λ_{em} = 510 (± 21) nm; Figure 2.1a]. Furthermore, the **DHIC**–Zn^{2+} complex could be applied to detect an anion, S^{2-}, among various anions (OAc^-, I^-, CN^-, F^-, S^{2-}, SCN^-, $H_2PO_4^-$, Br^-, B_2O^-, N_3^-, NO_2^-, and Cl^-). When S^{2-} (400 μM) was incubated with **DHIC**–Zn^{2+} for 1 h, the anion was able to interact with Zn^{2+} and consequentially sequester Zn^{2+} from **DHIC**. Therefore, we could observe a decrease in fluorescence using the GFP channel in the presence of S^{2-} (Figure 2.1b). These results demonstrate the potential ability of **DHIC** as a probe for detecting Zn^{2+} and S^{2-} in the biological system.

Scheme 2.1. A proposed mechanism of the **DHIC**–Zn^{2+} complex.

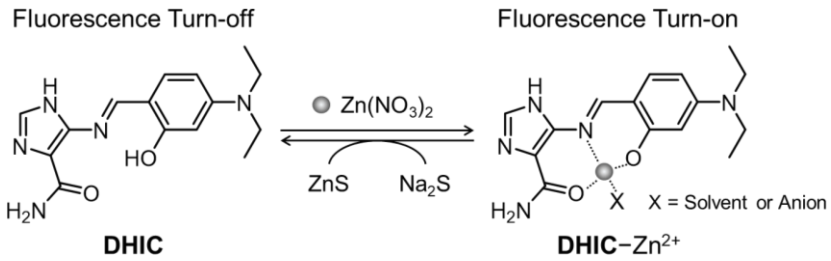

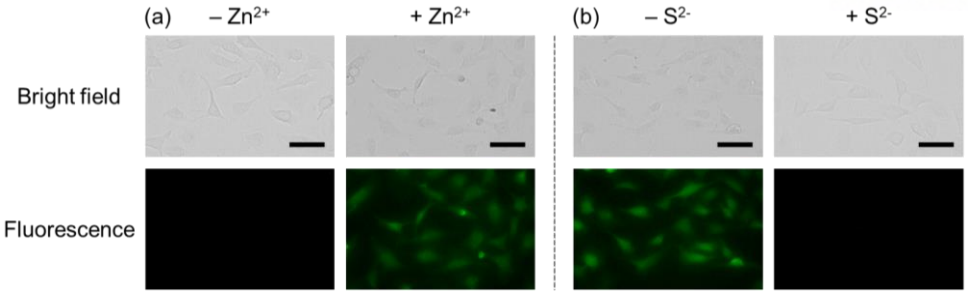

Figure 2.1. Fluorescent imaging of **DHIC** for Zn^{2+} with or without S^{2-} in HeLa cells. (a) The cells were pre-incubated with **DHIC** for 1 h prior to treatment with Zn^{2+}. (b) The cells incubated with **DHIC** for 1 h were treated with Zn^{2+} for 1 h. Conditions: [**DHIC**] = 20 μM; [Zn^{2+}] = 600 μM; [S^{2-}] = 400 μM; 37 °C; 5% CO_2. The scale bar is 50 μm.

2.2.2. Turn-on Fluorescent Probe, ATA-DAS, for Zn^{2+} in Living Cells

ATA-DAS was newly designed through the combination of thiophene and 4-(diethylamino)salicyl-aldehyde moieties. To investigate the fluorescent response of **ATA-DAS** to Zn^{2+} in living cells, fluorescence imaging experiments were conducted in HeLa cells. Our compound, **ATA-DAS** (30 μM), was simultaneously incubated with Zn^{2+} (5 mM) for 10 min with HeLa cells before taking fluorescence images. The fluorescence imaging of **ATA-DAS** in the presence of Zn^{2+} was observed at the GFP channel [λ_{ex} = 470 (± 11) nm; λ_{em} = 510 (± 21) nm; Figure 2.2]. In the presence of Zn^{2+}, the fluorescent response of **ATA-DAS** was noticeably increased. Thus, the results of our experiments suggest that **ATA-DAS** could be utilized as a chemosensor to detect Zn^{2+} in biological systems.

Scheme 2.2. A proposed mechanism of the **ATA-DAS**–Zn^{2+} complex.

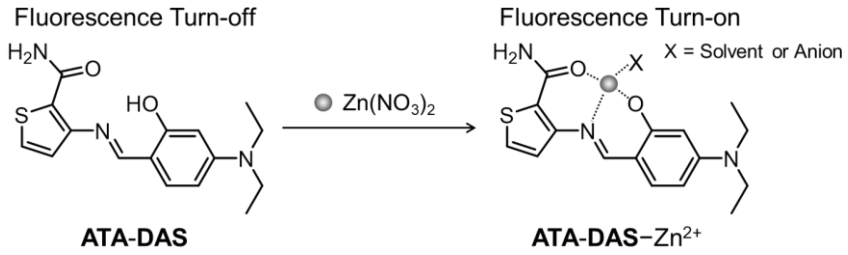

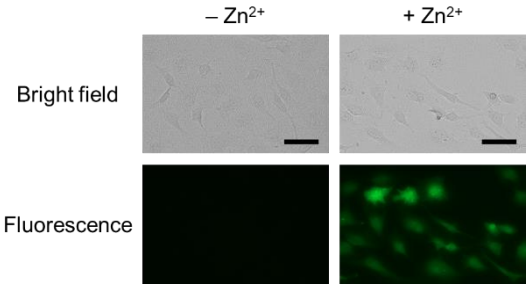

Figure 2.2. Fluorescent imaging of **ATA-DAS** for Zn^{2+} in HeLa cells. The cells were incubated with **ATA-DAS** and Zn^{2+} for 10 min. Conditions: [**ATA-DAS**] = 30 μM; [Zn^{2+}] = 5 mM; 37 °C; 5% CO_2. The scale bar is 50 μm.

2.2.3. Turn-on Fluorescent Probe, TPH-Jul, for Al^{3+} in Living Cells

TPH-Jul was rationally developed as a probe for Al^{3+} through the combination of thiophene and julolidine moieties. Upon incubation of **TPH-Jul** (10 μM) with various concentrations of Al^{3+} (*i.e.*, 0.25, 0.5, 1, and 1.5 mM) in living cells, a significant increase in fluorescence was visualized in a concentration-dependent manner. The cell imaging was conducted employing the GFP channel [λ_{ex} = 470 (± 11) nm; λ_{em} = 510 (± 21) nm; Figure 2.3]. Together, our results suggest the potential use of **TPH-Jul** as a sensor for Al^{3+} in biological systems.

Scheme 2.3. A proposed mechanism of the **TPH-Jul**–Al^{3+} complex.

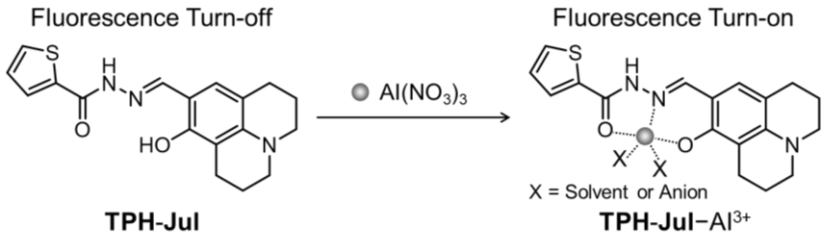

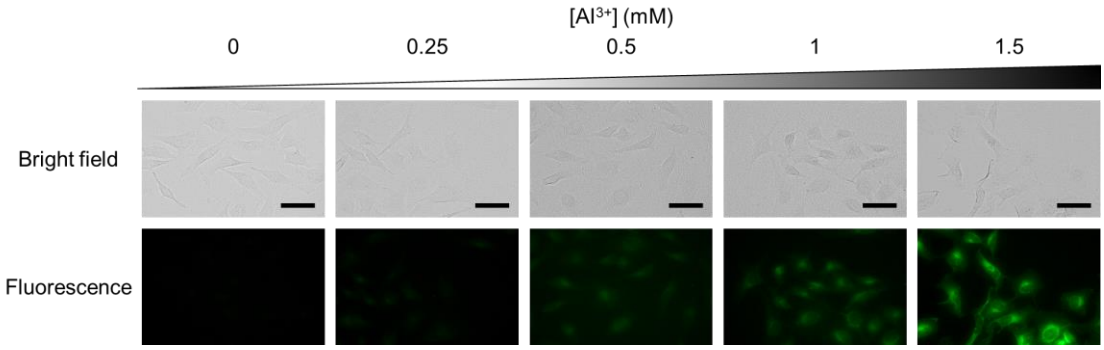

Figure 2.3. Fluorescent imaging of **TPH-Jul** for Al^{3+} in HeLa cells. The cells were incubated with **TPH-Jul** with various concentrations of Al^{3+} for 2 h. Conditions: [**TPH-Jul**] = 10 μM; [Al^{3+}] = 0.25, 0.5, 1, and 1.5 mM; 37 °C; 5% CO_2. The scale bar is 50 μm.

2.3. Conclusion

Dyshomeostasis of Zn^{2+} and Al^{3+} has been suggested to be related to the toxicity found in the AD-affected brain. In order to obtain a better understanding of the roles of metal ions in the pathology of AD, it would be valuable to have effective chemical probes able to selectively detect metal ions. In this Chapter, three fluorescent probes, **DHIC**, **ATA-DAS**, and **TPH-Jul**, were newly designed, and synthesized, and their ability to visualize metal ions [*i.e.*, Zn^{2+} (for **DHIC** and **ATA-DAS**) and Al^{3+} (for **TPH-Jul**)] was tested in living cells. In the near future, we will optimize their structures to improve their fluorescent responses to metal ions *in vitro* and in biological systems, as well as their properties for bioapplicability.

2.4. Experimental Section

2.4.1. Imaging Experiments in Living Cells

HeLa cells (ATCC, Manassas, USA) were maintained in media containing Dulbecco modified eagle medium (DMEM), 10% fetal bovine serum (FBS, GIBCO, Grand Island, NY, USA), 100 U/mL penicillin (GIBCO), and 100 mg/mL streptomycin (GIBCO). The cells were grown in a humidified atmosphere with 5% CO_2 at 37 °C. Cells were seeded onto 12 well plate (SPL Life Sciences, Pocheon, Gyeonggi-do, Republic of Korea) at a density of 10,000 cells per 100 μL and then incubated at 37 °C for 16 h. For imaging experiments, the cells were first treated with **DHIC** (DMSO; 1% v/v final DMSO concentration; 20 μM) for 1 h, before incubation with $Zn(NO_3)_2$ (10 mM bis-tris buffer, pH 7.43, 150 mM NaCl; 1% v/v final concentration; 600 μM) for 1 h. In addition, ii) **ATA-DAS** (DMSO; 1% v/v final DMSO concentration; 30 μM) or **TPH-Jul** (DMSO; 1% v/v final DMSO concentration; 10 μM) was incubated with $Zn(NO_3)_2$ (water; 1% v/v final concentration; 600 μM) for 10 min or $Al(NO_3)_3$ (water; 1% v/v final concentration; 0.25, 0.5, 1, and 1.5 mM) for 2 h, respectively. In case of fluorescence quenching experiments for **DHIC**, the cells were treated with **DHIC** (DMSO; 1% v/v final DMSO concentration; 20 μM) and $Zn(NO_3)_2$ (10 mM bis-tris buffer, pH 7.43, 150 mM NaCl; 1% v/v final concentration; 600 μM) for 1 h each. Na_2S (10 mM bis-tris buffer, pH 7.43, 150 mM NaCl; 1% v/v final concentration; 400 μM) was treated to the cells for 1 h. Imaging was performed with an EVOS FL fluorescence microscope (Life technologies) using a GFP light cube [for **DHIC**, **ATA-DAS**, and **TPH-Jul**; λ_{ex} = 470 (± 11) nm; λ_{em} = 510 (± 21) nm].

2.5. Acknowledgments

This work was supported by the National Research Foundation of Korea Grant funded by the Korean Government [NRF-2017R1A2B3002585 (to M.H.L)].

2.6. References

1. Bush, A. I.; Tanzi, R. E. *Neurotherapeutics* **2008**, *5*, 421-432.
2. Savelieff, M. G.; Lee, S.; Liu, Y.; Lim, M. H. *ACS Chem. Biol.* **2013**, *8*, 856-865.
3. Kepp, K. P. *Chem. Rev.* **2012**, *112*, 5193-5239.
4. Duce, J. A.; Bush, A. I. *Prog. Neurobiol.* **2010**, *92*, 1-18.
5. Que, E. L.; Domaille, D. W.; Chang, C. J. *Chem. Rev.* **2008**, *108*, 1517-1549.
6. Tomljenovic, L. *J. Alzheimers Dis.* **2011**, *23*, 567-598.
7. Nayak, P. *Environ. Res.* **2002**, *89*, 101-115.
8. Carter, K. P.; Young, A. M.; Palmer, A. E. *Chem. Rev.* **2014**, *114*, 4564-4601.
9. Yun, J. Y.; Chae, J. B.; Kim, M.; Lim, M. H.; Kim, C. *Photochem. Photobiol. Sci.* **2019**, Accepted for Publication.

Acknowledgment

I would like to thank people who have spent their time for supporting the completion of this thesis.

First of all, I would like to express my gratitude to my supervisor, Professor Mi Hee Lim, for her great support and guidance during my master's course. When I first came into this lab, I was afraid of English-speaking; however, I could improve my English skills. Thank Professor Lim for her care and encouragement. She has also given me an opportunity to have experience a variety of things, including experiments, writing scientific papers, and presentations like a scientist in public. In addition to those chances, in spite of her busy schedules, she spent valuable times for discussion and supervision about my research projects. Her guidance and directions have helped me to become a scientist capable of independently planning and conducting my research projects. Without her devotion, motivation, and mentoring, it would have been very difficult to finish my master's degree. I really appreciate her help and support, again.

Additionally, I would like to thank my co-advisor, Professor Oh-Hoon Kwon, for his acceptance of being my co-advisor. Without his support, I would not have been able to keep my status for a master's degree. I also appreciate my committee member, Professor Jung-Ming Kee, for taking the time to read my thesis and providing me helpful advice despite his busy schedule.

I also want to share my gratitude with great collaborators, Professor Joo-Yong Lee, Eunyoung Tak, Min Sun Kim, and Doin Kim. Without them, *in vivo* experiments, described in Chapter 1 of this thesis, would not be obtained.

I would like to extend my gratitude to the Lim group members, Dr. Hyuck Jin Lee, Juhye Kang, Geewoo Nam, Eunju Nam, Jiyeon Han, Yonghwan Ji, Misun Lee, Nahye Park, Jong-Min Suh, Yelim Yi, Gunhee Kim, Juri Lee, and Mina Son for their assistance, teaching, and scientific discussion. I also want to thank our lab manager, Mi Sook Lim, for her administration, encouragement, and guidance for our laboratory.

Lastly, I would like to thank my family [father (Gyeongju Kim), mother (Oksun Ryu), and brother (Seojun Kim)] for their encouragement and support that have given me the chance to achieve research achievements and finish my master's degree.

Mingeun Kim

Department of Chemistry
Ulsan National Institute of Science and Technology (UNIST)
50, UNIST-gil, Ulsan 44919, Republic of Korea
Email: mingeun0118@gmail.com

Education

Mar. 2017 – Present **M.S., Department of Chemistry, Ulsan National Institute of Science and Technology (UNIST), Ulsan, Republic of Korea**
Advisors: Professors Mi Hee Lim & Oh-Hoon Kwon

Mar. 2011 – Feb. 2017 **B.S., Department of Chemistry, Pukyong National University, Busan, Republic of Korea**
Graduated *Summa Cum Laude*

Honors, Awards, and Scholarships

Mar. 2017 – Feb. 2018 **Teaching Assistant (TA) Scholarship**
Ulsan National Institute of Science and Technology (UNIST), Ulsan, Republic of Korea

Feb. 2017 **Korean Chemical Society President's Award**
Seoul, Republic of Korea

Feb. 2017 **Natural Science College Dean's Award**
Pukyong National University, Busan, Republic of Korea

Feb. 2016 **Natural Science College Dean's Award**
Pukyong National University, Busan, Republic of Korea

Jan. 2015 **College Educational Development Institute Director's Award**
Pukyong National University, Busan, Republic of Korea

Mar. 2014 – Feb. 2017 **Daehwa Scholarship Society**
Pukyong National University, Busan, Republic of Korea

Professional Activity

Jan. 2015 – Dec. 2015 **Student President**
Pukyong National University, Busan, Republic of Korea

Jan. 2014 – Jun. 2016 **Bachelor's Work**
Pukyong National University, Busan, Republic of Korea

Research Experience

Mar. 2017 – Present Graduate Student
Ulsan National Institute of Science and Technology (UNIST), Ulsan, Republic of Korea
Advisor: Professor Mi Hee Lim
Research Topic:
(a) Development of Chemical Reagents to Modulate Multiple pathogenic factors found in Alzheimer's Disease
(b) Monitoring Amyloid-β aggregates by Fluorescent Probes *in Vitro*
(c) Detection of Metal Ions by Fluorescent Sensors in Living Cells

Jul. 2016 – Feb. 2017 Visiting Student
Ulsan National Institute of Science and Technology (UNIST), Ulsan, Republic of Korea
Advisor: Professor Mi Hee Lim
Research Topic: Development of Chemical Reagents to Modulate Multiple pathogenic factors found in Alzheimer's Disease

Teaching Experience

Mar. 2017 – Feb. 2018 General Chemistry Laboratory, Teaching Assistant
Department of Chemistry
Ulsan National Institute of Science and Technology (UNIST), Ulsan, Republic of Korea

Publications

Submitted or In Revision

7. **Mingeun Kim**,† Juhye Kang,† Misun Lee,† Jiyeon Han, Geewoo Nam, Eunyoung Tak, Min Sun Kim, Doin Kim, Hyuck Jin Lee, Eunju Nam, Joo-Yong Lee,* and Mi Hee Lim* *Manuscript in Preparation*.
"Minimalistic Design Approach for Multi-Reactivity against Free Radicals and Metal-Free and Metal-Bound Amyloid-β Peptides: Redox-Based Substitutions of Benzene"

6. Misun Lee,† Min Hee Park,† Ju Youn Lee, Min Seock Jeong, Kang Ho Park, Seung Hoon Han, **Mingeun Kim**, Juhye Kang, Geewoo Nam, Eunyoung Tak, Min Sun Kim, Joo-Young Lee, Hee Kyung Jin,* Jae-Sung Bae,* and Mi Hee Lim* *Submitted for Publication* (†Co-first authorship).
"A Neuroprotective Small Molecules Promotes Microglial Phagocytic Aptitude and Improves Cognitive Function"

5. Dongju Yun, Ji Hye Kang, Min Seon Kim, **Mingeun Kim**, Mi Hee Lim, and Cheal Kim* *Submitted for Publication*.
"A Multiple Target Chemosensor: Fluorescent Detection of Al(III) and Colorimetric Detection of Fe(II) and Cu(II)"

4. Min Seon Kim, Dongju Yun, Ju Chae, Hyojin Lee, **Mingeun Kim**, Mi Hee Lim, Cheal Kim, and Ki-Tae Kim* *Submitted for Publication*.
"A Fluorescent Turn-on Chemosensor Based on Thiophene for the Detection of Zn^{2+} and CN^{-}: Applications for Imaging in Living Cells and Zebrafish"

Published or In Press

3. Jin Yeong Yun, Ju Byeong Chae, **Mingeun Kim**, Mi Hee, Lim, and Cheal Kim* *Photochem. Photobiol. Sci.* **2019**, *In Press*.
"A Multiple Target Chemosensor for the Sequential Fluorescence Detection of Zn^{2+} and S^{2-} and the Colorimetric Detection of $Fe^{3+/2+}$ in Aqueous Media and Living Cells"

2. Misun Lee,† **Mingeun Kim**,† Anjong Florence Tikum,† Hyuck Jin Lee, Vijayan Thamilarasan, Mi Hee Lim,* and Jinheung Kim* *Dyes Pigm.* **2019**, *162*, 97-103 (†Co-first authorship).
"A Near-infrared Fluorescent Probe for Amyloid-β Aggregates"

1. Michael W. Beck, Jeffrey S. Derrick, Jong-Min Suh, **Mingeun Kim**, Kyle J. Korshavn, Richard A. Kerr, Woo Jong Cho, Scott D. Larsen, Brandon T. Ruotolo, Ayyalusamy Ramamoorthy,* and Mi Hee Lim* *ChemMedChem* **2017**, *12*, 1828-1838.
"Minor Structural Variations of Small Molecules Tune Regulatory Activities toward Pathological Factors in Alzheimer's Disease"

**Note: This paper was selected as "Front Cover"*

Presentations

2. **Poster**, 122nd General Meeting of the Korean Chemical Society, October 17-19, 2018, Daegu, Republic of Korea
Mingeun Kim and Mi Hee Lim*
"Minor Structural Variations of Small Molecules Tune Regulatory Activities toward Pathological Factors in Alzheimer's Disease"

1. **Poster**, 2018 Inorganic Chemistry Symposium, June 28-29, 2018, Busan, Republic of Korea
Mingeun Kim and Mi Hee Lim*
"Minor Structural Variations of Small Molecules Tune Regulatory Activities toward Pathological Factors in Alzheimer's Disease"

Technical Skills

Organic synthesis, spectroscopic studies (NMR, UV–Vis, fluorescence), mass spectrometric studies (MS), gel electrophoresis, Western blot, and mammalian cell culture.